International Journal of Mechanical Sciences 258 (2023) 108551

Contents lists available at ScienceDirect

International Journal of Mechanical Sciences

journal homepage: www.elsevier.com/locate/ijmecsci

The optimal design of negative stiffness inerter passive dampers for structures

Sudip Chowdhury [a,*], Arnab Banerjee [a], Sondipon Adhikari [b]

[a] Civil Engineering Department, Indian Institute of Technology Delhi, India
[b] James Watt School of Engineering, The University of Glasgow, Glasgow, Scotland, UK

ARTICLE INFO

Keywords:
Negative stiffness passive vibration control devices
Negative stiffness inerter-based base isolators (NSIBI)
Negative stiffness base isolators (NSBI)
Negative stiffness inerter-based tuned mass dampers (NSITMD)
Negative stiffness tuned mass dampers (NSTMD)
Exact closed-form expressions

ABSTRACT

The combination of negative stiffness devices and inerters to traditional base isolators (TBI) and tuned mass dampers (TMD) does not exist in any state-of-the-art. Therefore, to pursue the research using the above-mentioned research scope, the negative stiffness inerter passive dampers such as negative stiffness inerter-based base isolators (NSIBI), negative stiffness base isolators (NSBI), negative stiffness inerter-based tuned mass dampers (NSITMD), and negative stiffness tuned mass dampers (NSTMD) are introduced in this paper. H_2 and H_∞ optimization methods are applied to derive the exact closed-form expressions for the optimal design parameters of these novel passive vibration dampers. Newton's second law applies to derive the governing equations of motion of the controlled structures. The transfer function formation and Newmark-beta method are applied to determine the dynamic responses of the controlled structures analytically and numerically. Hence, H_2 optimized NSIBI and NSBI have 45.98% and 46.71% more dynamic response reduction capacities than optimum TBI. In addition, H_∞ optimized NSIBI and NSBI have 58.36% and 57.32% more dynamic response reduction capacities than optimum TBI. Furthermore, the optimum NSITMD and NSTMD have 0.42%, 10.84%, and 4.5%, 13.48% more dynamic response reduction capacities than traditional TMD. All the derivations are mathematically accurate.

1. Introduction

Passive vibration control systems are built to protect structures and living creatures from natural disasters like earthquakes and cyclones. These devices are the most economical and immensely studied vibration control devices globally. The base isolators (BI) [1] are prominent due to their superior vibration reduction capacities among the passive dampers. However, the base isolators are inefficient for high-rise buildings to reduce the dynamic responses. To overcome this drawback, tuned mass dampers (TMD) are installed [2] at the top of high-rise buildings [3]. BI mechanism was introduced by Touaillon in 1870, and since then, it has been studied immensely [4]. BI is installed in between the superstructure and substructures of many aeronautical [5], mechanical [6], and civil engineering structures [7]. BI is installed in the building structures to reduce the inter-story drift [8] and accelerations [9]. New Zealand bearings [10], lead rubber bearings [11], resilient friction base isolators [12], friction-pendulum systems [13], and pure-friction systems [14] are the nonlinear BI [15] available in the industry.

Frahm introduced TMD in 1909 without considering the damping [16]. An undamped TMD is effective when the TMD's inherent frequency is near the excitation frequency. However, no vibration decreases when the excitation frequency differs from the TMD's native frequency [17]. Therefore, to overcome this drawback, Ormondroyd and Den Hartog introduced damping inside the core material of TMD. They also have provided optimal closed-form solutions for the design parameters [18].

To achieve these optimal design parameters regarding closed-form expressions, H_2 and H_∞ optimization methods are introduced [19]. H_2 optimization method applies to structures excited by random white noises [20]. The standard deviations of the dynamic responses of the controlled structures are reduced using H_2 optimized [21] dampers [22]. In contrast, the maximum amplitudes of the dynamic responses of the controlled structures are reduced using H_∞ dampers [2]. The optimization method applies to harmonically excited controlled structures. This method was first introduced by Den Hartog in 1985 by introducing a book, namely "Mechanical Vibration" [23]. However, the optimal closed-form solutions for the design parameters of the dampers need to be presented in a more detailed manner. In addition, the previously established closed-form expressions' accuracy for optimal design parameters must be cross-checked [24]. Traditionally, the dynamic response reduction capacities of the base isolators and tuned mass dampers are enhanced by increasing the static mass of the dampers. However, increasing the static mass of the damper enhances its flexibility as the natural frequency of the dampers reduces.

* Corresponding author.
E-mail address: sudip.chowdhury@civil.iitd.ac.in (S. Chowdhury).

https://doi.org/10.1016/j.ijmecsci.2023.108551
Received 20 October 2022; Received in revised form 12 June 2023; Accepted 12 June 2023
Available online 19 June 2023

Therefore, the time period of the damper increases. Sometimes, for high amplitude vibrations, the time period of the dampers enlarges extensively, which causes damage to the structural configurations of the dampers. Precisely, the load-bearing capacity of the controlled structure reduces. The adaptability of the dampers is reduced for the changing pattern of the ground motions, i.e., from near-fault to far-field. In contrast, to increase the static mass of the dampers, the number of tuned mass dampers needs to be increased to reduce the dynamic responses of the structures. As a result, the total static mass of the damper array rises, increasing the cost. Hence, instead of static mass, the effective mass of the dampers needs to be increased.

Recently, Smith [25] introduced inerters, the effective mass amplification device through the force to the current analogy for mitigation of dynamic responses of the dynamic systems [26]. Other researchers are also studied different mass amplification, negative stiffness, negative mass, and different mechanical devices for increasing the dynamic response reduction capacity of conventional passive vibration isolation devices [27]. Inertial amplifiers [28–30] are one of the mass amplification devices which can provide large wide-bandgap at low frequencies [31] and these characteristics allow this device to apply in the civil engineering structures. The inerters are also implanted inside or parallel to the conventional passive vibration control devices to increase their energy dissipation capacity by amplifying the significant effective mass through rotational mass with motion transformers inside the system [32]. The inerters are applied to mechanical engineering fields to reduce the mechanical responses of the structures [33]. The inerters are also applied in civil engineering structures [34] to minimize the dynamic responses of the structures. Inerters are implanted in the core material of TMD [35] and BI to mitigate the responses of dynamic systems, such as buildings, wind turbines, and bridges [36].

Instead of effective mass amplification devices, different types of negative stiffness devices such as quasi-zero stiffness [37], high-static-low-dynamic stiffness [38], Euler buckled beams as negative stiffness elements [39], pseudo-negative-stiffness [40], negative-stiffness inclusions [41], magnetic negative stiffness dampers [42] are installed inside the passive vibration isolation systems to increase their vibration reduction capacities. However, a minimal number of applications for entire structures are observed for inerters such as buildings and bridges. KDamper-based devices can be considered as an extension of the conventional TMD concept by the introduction of an appropriate negative stiffness element to the additional mass of the TMD [43,44]. These devices can be thus considered as an indirect approach to increase the inertia effect of the additional mass with the negative stiffness element force without, however, having to directly increase the additional mass itself [45,46]. However, from the existing state of the art, it has been observed that the implantation of negative stiffness devices (NSD), inerters inside the core material of the passive vibration control devices such as base isolators (BI) and tuned mass dampers (TMD) to increase their dynamic response reduction capacities are minimal [47]. Precisely, the combination of negative stiffness devices (NSD) and inerters to BI and TMD do not exist in any state of the art. In addition, the optimal design parameters for the above-mentioned novel dampers in terms of closed-form expressions also do not exist. Therefore, a research scope has been found.

Therefore, to pursue the research using the above-mentioned research scope, the negative stiffness inerter-based base isolators (NSIBI), negative stiffness base isolators (NSBI), negative stiffness inerter-based tuned mass dampers (NSITMD), and negative stiffness tuned mass dampers (NSTMD) are introduced in this paper. These novel dampers are installed in single-degree-of-freedom systems (SDOF), having the same system parameters, such as damping ratio $\zeta_s = 0.05$, to reduce their dynamic responses subjected to base excitations. H_2 and H_∞ optimization methods are applied to derive the optimal design parameters for these novel passive vibration isolation systems in terms of closed-form expressions. These optimal closed-form solutions are provided maximum vibration reduction capacity to the novel dampers. Newton's second law applies to derive the governing equations of motion for the controlled structures subjected to base excitations. The transfer function formation and Newmark-beta method are applied to determine the dynamic responses of the controlled structures analytically and numerically. The near-field earthquake records are applied to the base of the controlled structures. The maximum dynamic responses of the structures controlled by novel dampers are compared with the maximum dynamic responses of the structures controlled by conventional dampers.

Table 1
The values of inerter masses for NSIBI and NSBI.

Mass	NSIBI	NSBI
m_d	$m_d \neq 0$	$m_d = 0$

2. Novel base isolators

The values of inerter masses for NSIBI and NSBI are listed in Table 1. The structural diagram of SDOF systems isolated by novel isolators is displayed in Fig. 1(a). The schematic diagrams of NSIBI and NSBI are shown in Figs. 1(b) and 1(c). m_b, k_b, and c_b define the mass, stiffness, and damping of novel isolators. m_d defines the inerter mass. k_d defines the negative stiffness of the novel isolators, i.e., $k_d = \beta k_b$. $\ddot{x}_g$ defines the base excitation. m_s, k_s, and c_s define the mass, stiffness, and damping of SDOF systems. u_s and u_b define the absolute dynamic response of SDOF systems and novel isolators. NSBI is mathematically formulated by considering $m_d = 0$. Newton's second law applies to derive the governing equations of motion of the SDOF systems isolated by the novel isolators, such as NSIBI and NSBI subjected to base excitation and expressed as

$$\begin{aligned} m_s\ddot{x}_s + m_s\ddot{x}_b + c_s\dot{x}_s + k_s x_s &= -m_s\ddot{x}_g, \\ m_b\ddot{x}_b + m_d\ddot{x}_b + c_b\dot{x}_b + k_e x_b - k_s x_s - c_s\dot{x}_s &= -m_b\ddot{x}_g, \end{aligned} \tag{1}$$

where $k_e = k_b - k_d$ defines the total effective stiffness of NSIBI, $x_b = u_b - x_g$ and $x_s = u_s - u_b$ define to the relative dynamic responses of the isolator and main structure. $c_s = 2\,m_s\zeta_s\omega_s$ and $k_s = m_s\omega_s^2$ are the damping and stiffness of the SDOF systems. $c_b = 2\zeta_b(m_b + m_d)\omega_b$ and $k_b = (m_b + m_d)\omega_b^2$ are the damping and stiffness of novel dampers. $x_s = X_s e^{i\omega t}$, $x_b = X_b e^{i\omega t}$, and $\ddot{x}_g = A_g e^{i\omega t}$ are the steady state solutions, applying to Eq. (1). Therefore, the transfer function obtains as

$$\begin{bmatrix} 2\zeta_s q\omega_s + q^2 + {\omega_s}^2 & q^2 \\ -2\zeta_s q\omega_s - {\omega_s}^2 & (\mu_b + \mu_d)\left((1-\beta){\omega_b}^2 + 2\zeta_b q\omega_b + q^2\right) \end{bmatrix} \times \begin{Bmatrix} X_s \\ X_b \end{Bmatrix} = -\begin{bmatrix} 1 \\ \mu_b \end{bmatrix} A_g, \tag{2}$$

where $\beta = k_d/k_b$ defines the negative stiffness ratio of the novel isolators. The dynamic responses of the SDOF system and NSIBI determine as

$$H_s(q) = \frac{X_s}{A_g} = \frac{\begin{array}{c} -\beta\,\mu_b{\omega_b}^2 - \beta\,\mu_d{\omega_b}^2 + 2\,q\zeta_b\mu_b\omega_b \\ +2\,q\zeta_b\mu_d\omega_b + q^2\mu_d + \mu_b{\omega_b}^2 + \mu_d{\omega_b}^2 \end{array}}{\Delta}, \tag{3}$$

$$H_b(q) = \frac{X_b}{A_g} = \frac{2\,\zeta_s q\omega_s\mu_b + q^2\mu_b + 2\,\zeta_s q\omega_s + {\omega_s}^2\mu_b + {\omega_s}^2}{\Delta}. \tag{4}$$

The denominator (Δ) of the dynamic response function is separated into its real and imaginary parts as obtains as

$$\begin{aligned} \Delta = {} & \begin{array}{c} 2\,\beta\,q\zeta_s\mu_b{\omega_b}^2\omega_s + 2\,\beta\,q\zeta_s\mu_d{\omega_b}^2\omega_s - 4\,q^2\zeta_b\zeta_s\mu_b\omega_b\omega_s - 4\,q^2\zeta_b\zeta_s\mu_d\omega_b\omega_s \\ +\beta\,q^2\mu_b{\omega_b}^2 + \beta\,q^2\mu_d{\omega_b}^2 + \beta\,\mu_b{\omega_b}^2{\omega_s}^2 + \beta\,\mu_d{\omega_b}^2{\omega_s}^2 - 2\,q^3\zeta_b\mu_b\omega_b \\ -2\,q^3\zeta_b\mu_d\omega_b - 2\,q^3\zeta_s\mu_b\omega_s - 2\,q^3\zeta_s\mu_d\omega_s - 2\,q\zeta_b\mu_b\omega_b{\omega_s}^2 - 2\,q\zeta_b\mu_d\omega_b{\omega_s}^2 \\ -2\,q\zeta_s\mu_b{\omega_b}^2\omega_s - 2\,q\zeta_s\mu_d{\omega_b}^2\omega_s - q^4\mu_b - q^4\mu_d - 2\,q^3\zeta_s\omega_s - q^2\mu_b{\omega_b}^2 \\ -q^2\mu_b{\omega_s}^2 - q^2\mu_d{\omega_b}^2 - q^2\mu_d{\omega_s}^2 - \mu_b{\omega_b}^2{\omega_s}^2 - \mu_d{\omega_b}^2{\omega_s}^2 - q^2{\omega_s}^2. \end{array} \end{aligned} \tag{5}$$

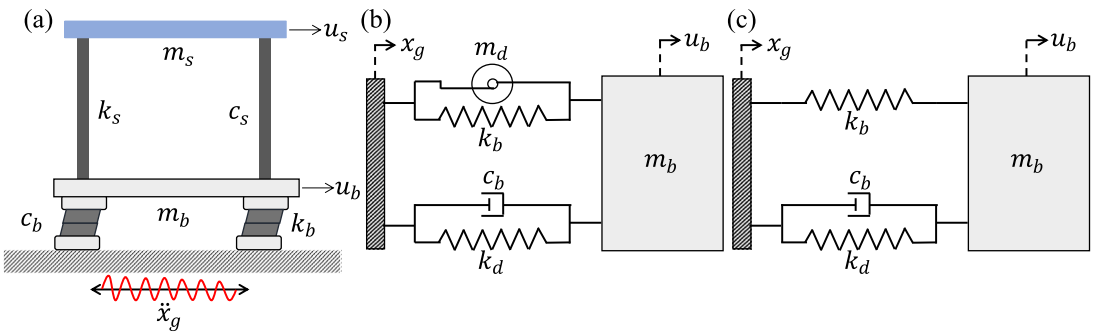

Fig. 1. (a) The structural diagram of SDOF systems isolated by novel negative stiffness base isolators. The schematic diagrams of (b) negative stiffness inerter-based base isolation system and (c) Negative stiffness base isolation system.

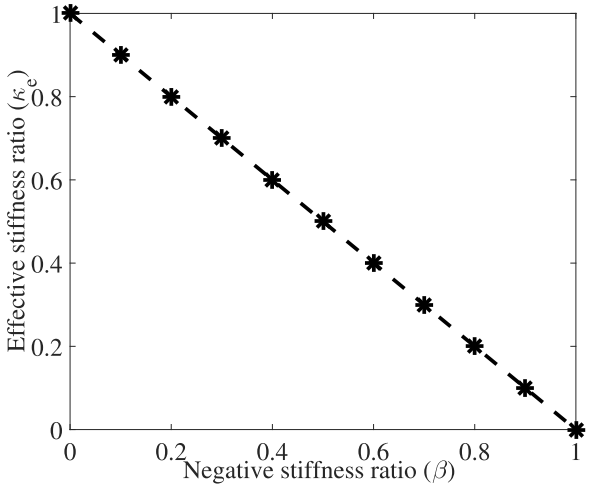

Fig. 2. The difference in effective stiffness ratio versus negative stiffness ratio of NSBI.

The total effective mass of NSIBI obtains as $m_e = m_b + m_d$. Accordingly, the effective mass and stiffness ratios derive as

$$\mu_e = \frac{m_b + m_d}{m_s} = \mu_b + \mu_d, \qquad \kappa_e = \frac{k_b - k_d}{k_b} = \frac{(\mu_b + \mu_d)(1-\beta)}{\mu_b}, \tag{6}$$

where $\beta = k_d/k_b$ defines the novel isolators' negative stiffness ratio. Considering $\mu_d = 0$, the total effective stiffness of NSBI derives as

$$k_e = k_b - k_d = k_b(1-\beta), \tag{7}$$

where $k_d = \beta k_b$ defines to the negative stiffness of NSBI. The effective stiffness ratio w.r.t the static stiffness of the NSBI derives as

$$\kappa_e = \frac{k_b - k_d}{k_b} = (1-\beta). \tag{8}$$

The difference in the effective stiffness ratio versus the negative stiffness ratio of NSBI is shown in Fig. 2. The effective stiffness decreases as the negative stiffness ratio of NSBI increases. A higher stiffness ratio provides a more flexible base to the isolated structures, increasing the isolator's dynamic response reduction capacity.

3. H_2 optimization for NSIBI and NSBI systems

H_2 optimization employs to derive the optimal design parameters for NSIBI and NSBI subjected to random-white noise excitation [19,20]. $\zeta_s = 0$ considers to perform this optimization. A mathematical expression with the matrices is derived to obtain the standard deviation (SD) of the dynamic responses of the isolated structures and expressed as

$$\sigma^2_{x_{s,b}} = \int_{-\infty}^{\infty} \frac{\Xi_n(\omega)\,\mathrm{d}\omega}{\Lambda_n(\mathrm{i}\omega)\Lambda_n^*(\mathrm{i}\omega)} = \frac{\pi}{a_4}\frac{\det[\mathbf{N}_4]}{\det[\mathbf{D}_4]}, \tag{9}$$

$$N_4 = \begin{bmatrix} b_3 & b_2 & b_1 & b_0 \\ -a_4 & a_2 & -a_0 & 0 \\ 0 & -a_3 & a_1 & 0 \\ 0 & a_4 & -a_2 & a_0 \end{bmatrix} \quad \text{and} \quad D_4 = \begin{bmatrix} a_3 & -a_1 & 0 & 0 \\ -a_4 & a_2 & -a_0 & 0 \\ 0 & -a_3 & a_1 & 0 \\ 0 & a_4 & -a_2 & a_0 \end{bmatrix}. \tag{10}$$

The SD of the main structure derives as

$$\sigma^2_{x_s} = \frac{S_0\pi \begin{pmatrix} \beta^2\mu_b{}^2\omega_b{}^4 + 2\beta^2\mu_b\mu_d\omega_b{}^4 + \beta^2\mu_d{}^2\omega_b{}^4 + 4\zeta_b{}^2\mu_b{}^2\omega_b{}^2\omega_s{}^2 \\ +4\zeta_b{}^2\mu_d{}^2\omega_b{}^2\omega_s{}^2 - 2\beta\mu_b{}^2\omega_b{}^4 - 4\beta\mu_b\mu_d\omega_b{}^4 + 2\beta\mu_b\mu_d\omega_b{}^2\omega_s{}^2 \\ -2\beta\mu_d{}^2\omega_b{}^4 + 2\beta\mu_d{}^2\omega_b{}^2\omega_s{}^2 - \beta\mu_b\omega_b{}^2\omega_s{}^2 - \beta\mu_d\omega_b{}^2\omega_s{}^2 \\ +\mu_b{}^2\omega_b{}^4 + 2\mu_b\mu_d\omega_b{}^4 - 2\mu_b\mu_d\omega_b{}^2\omega_s{}^2 + \mu_d{}^2\omega_b{}^4 - 2\mu_d{}^2\omega_b{}^2\omega_s{}^2 \\ +\mu_d{}^2\omega_s{}^4 + \mu_b\omega_b{}^2\omega_s{}^2 + \mu_d\omega_b{}^2\omega_s{}^2 + 8\zeta_b{}^2\mu_b\mu_d\omega_b{}^2\omega_s{}^2 \end{pmatrix}}{2\,\omega_b\zeta_b\,(\mu_b+\mu_d)\,\omega_s{}^6}. \tag{11}$$

To derive optimal design parameters, Eq. (11) is partially differentiated w.r.t the damping ratio and frequency of NSIBI and expressed as

$$\frac{\partial\sigma^2_{x_s}}{\partial\zeta_b} = 0 \quad \text{and} \quad \frac{\partial\sigma^2_{x_s}}{\partial\omega_b} = 0. \tag{12}$$

The first equation of Eq. (12) is substituted by Eq. (11). The damping ratio of NSIBI is derived as

$$\zeta_b = \sqrt{\frac{\beta^2\mu_b{}^2\omega_b{}^4 + 2\beta^2\mu_b\mu_d\omega_b{}^4 + \beta^2\mu_d{}^2\omega_b{}^4 - 2\beta\mu_b{}^2\omega_b{}^4 - 4\beta\mu_b\mu_d\omega_b{}^4 \\ +2\beta\mu_b\mu_d\omega_b{}^2\omega_s{}^2 - 2\beta\mu_d{}^2\omega_b{}^4 + 2\beta\mu_d{}^2\omega_b{}^2\omega_s{}^2 - \beta\mu_b\omega_b{}^2\omega_s{}^2 \\ -\beta\mu_d\omega_b{}^2\omega_s{}^2 + \mu_b{}^2\omega_b{}^4 + 2\mu_b\mu_d\omega_b{}^4 - 2\mu_b\mu_d\omega_b{}^2\omega_s{}^2 \\ +\mu_d{}^2\omega_b{}^4 - 2\mu_d{}^2\omega_b{}^2\omega_s{}^2 + \mu_d{}^2\omega_s{}^4 + \mu_b\omega_b{}^2\omega_s{}^2 + \mu_d\omega_b{}^2\omega_s{}^2}{4\mu_b{}^2\omega_b{}^2\omega_s{}^2 + 8\mu_b\mu_d\omega_b{}^2\omega_s{}^2 + 4\mu_d{}^2\omega_b{}^2\omega_s{}^2}}. \tag{13}$$

To derive modified SD, Eq. (13) is substituted in Eq. (11). Hence, the SD is modified as

$$\sigma^2_{x_s} = \sqrt{\frac{(\mu_b+\mu_d)^2(\beta-1)^2\omega_b{}^4 + \mu_d{}^2\omega_s{}^4 \\ +2\,(\mu_b+\mu_d)\,\omega_s{}^2\,(\mu_d - 1/2)\,(\beta-1)\,\omega_b{}^2}{\omega_b{}^2\omega_s{}^2\,(\mu_b+\mu_d)^2}}\,(\mu_b+\mu_d)\,\omega_s{}^6\omega_b. \tag{14}$$

To derive natural frequency of NSIBI, Eq. (14) is substituted in the second expression of Eq. (12). The optimal natural frequency of NSIBI is derived as

$$(\omega_b)_{\mathrm{opt}} = \frac{\sqrt{2\,(\mu_b+\mu_d-\beta\,\mu_b-\beta\,\mu_d)\,(1-2\,\mu_d)}\,\omega_s}{2\,(\mu_b+\mu_d-\beta\,\mu_b-\beta\,\mu_d)}. \tag{15}$$

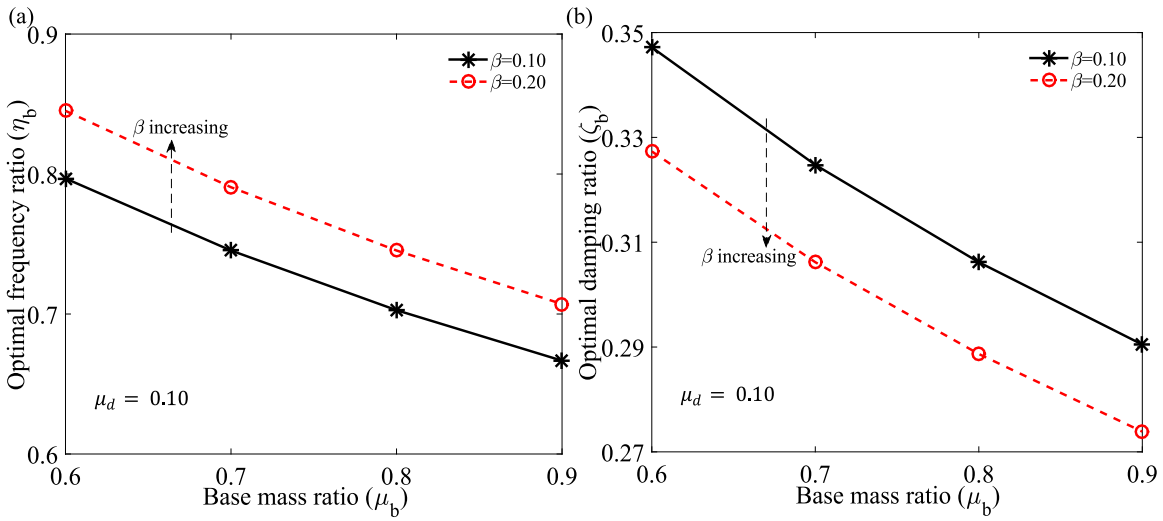

Fig. 3. (a) The differences in optimal frequency ratio η_b versus base mass ratio μ_b for different values of negative stiffness ratio β of NSIBI. The black solid ($\beta = 0.10$) and red dashed ($\beta = 0.20$) lines with markers are employed to address these plots. (b) The differences in optimal damping ratio ζ_b versus base mass ratio μ_b for different values of negative stiffness ratio β of NSIBI. The black solid ($\beta = 0.10$) and red dashed ($\beta = 0.20$) lines with markers are employed to address these plots. $\mu_d = 0.1$ is applied for both graphs.

The non-dimensional form of the optimal frequency ratio of NSIBI is derived using Eq. (15) and expressed as

$$(\eta_b)_{\text{opt}} = \frac{\sqrt{2\left(\mu_b+\mu_d-\beta\,\mu_b-\beta\,\mu_d\right)\left(1-2\,\mu_d\right)}}{2\left(\mu_b+\mu_d-\beta\,\mu_b-\beta\,\mu_d\right)}. \tag{16}$$

The optimal damping ratio of NSIBI is derived by substituting Eq. (15) in Eq. (13) and expressed as

$$(\zeta_b)_{\text{opt}} = \frac{\sqrt{2}}{4}\sqrt{\frac{\left(1-4\,\mu_d\right)(1-\beta)}{\left(1-2\,\mu_d\right)\left(\mu_b+\mu_d\right)}}. \tag{17}$$

The differences in optimal frequency and damping ratios versus the base mass ratio for different values of negative stiffness ratio of NSIBI are displayed in Figs. 3(a) and 3(b). To obtain Fig. 3, Eqs. (16) and (17) are employed. $\mu_d \neq 0$ is considered for NSIBI. The frequency and damping ratios decrease with the increment of the base mass ratio. In contrast, the frequency ratio increase and the damping ratio decrease with the increment of the negative stiffness ratio. Substituting $\mu_d = 0$ in Eqs. (16) and (17), the exact closed-form expressions for the optimal frequency and damping ratios of NSBI are derived. The differences in optimal frequency and damping ratios versus the base mass ratio for different values of negative stiffness ratio of NSBI are displayed in Figs. 4(a) and 4(b). The frequency and damping ratios decrease with the increment of the base mass ratio. In contrast, the frequency ratio increase and the damping ratio decrease with the increment of the negative stiffness ratio.

4. H_∞ optimization for NSIBI and NSBI

H_∞ optimization is employed to derive the optimal design parameters for NSIBI and NSBI subjected to harmonic excitation [19,20]. $\zeta_s = 0$ considers to perform this optimization. The dimensional transfer function in Eq. (2) is transformed into a non-dimensional transfer function and expressed as

$$\begin{bmatrix} -\eta^2+2\mathrm{i}\zeta_s\eta+1 & -\eta^2 \\ -2\mathrm{i}\zeta_s\eta-1 & B_{12} \end{bmatrix}\begin{Bmatrix} X_s \\ X_b \end{Bmatrix} = -\begin{bmatrix} 1 \\ \mu_b \end{bmatrix}\frac{A_g}{\omega_s^2}, \tag{18}$$

$$B_{12} = \left(\mu_b+\mu_d\right)\left(2\mathrm{i}\zeta_b\eta\,\eta_b-\beta\,{\eta_b}^2-\eta^2+{\eta_b}^2\right).$$

The dynamic response of the main structure derives as

$$H_s(\eta) = \frac{X_s}{A_g}\omega_s^2 = \frac{-\beta\,{\eta_b}^2\mu_b-\beta\,{\eta_b}^2\mu_d-\eta^2\mu_d+{\eta_b}^2\mu_b+{\eta_b}^2\mu_d+2\,\mathrm{i}\zeta_b\eta\,\eta_b\left(\mu_b+\mu_d\right)}{\Delta}. \tag{19}$$

The dynamic response of NSIBI derives as

$$H_b(\eta) = \frac{X_b}{A_g}\omega_s^2 = \frac{-\eta^2\mu_b+\mu_b+1+2\,\mathrm{i}\eta\,\zeta_s\left(\mu_b+1\right)}{\Delta}. \tag{20}$$

The denominator (Δ) of the dynamic response function is separated into its real and imaginary parts as obtains as

$$\begin{aligned}\Delta = {} & \eta^2-\beta\,\eta^2{\eta_b}^2\mu_b-\beta\,\eta^2{\eta_b}^2\mu_d+4\,\eta^2\zeta_b\zeta_s\eta_b\mu_b+4\,\eta^2\zeta_b\zeta_s\eta_b\mu_d-\eta^4\mu_b-\eta^4\mu_d \\ & +\eta^2{\eta_b}^2\mu_b+\eta^2{\eta_b}^2\mu_d+\beta\,{\eta_b}^2\mu_b+\beta\,{\eta_b}^2\mu_d+\eta^2\mu_b+\eta^2\mu_d-{\eta_b}^2\mu_b-{\eta_b}^2\mu_d \\ & +\mathrm{i}\left(\begin{array}{c} 2\,\beta\,\eta\,\zeta_s{\eta_b}^2\mu_b+2\,\beta\,\eta\,\zeta_s{\eta_b}^2\mu_d+2\,\eta^3\zeta_b\eta_b\mu_b+2\,\eta^3\zeta_b\eta_b\mu_d+2\,\eta^3\zeta_s\mu_b \\ +2\,\eta^3\zeta_s\mu_d-2\,\eta\,\zeta_s{\eta_b}^2\mu_b-2\,\eta\,\zeta_s{\eta_b}^2\mu_d+2\,\eta^3\zeta_s-2\,\eta\,\zeta_b\eta_b\mu_b \\ -2\,\eta\,\zeta_b\eta_b\mu_d \end{array}\right),\end{aligned} \tag{21}$$

where $\eta = \omega/\omega_s$ defines excitation frequency. The resultant of Eq. (20) is conceptualized as

$$|\,H_s(\eta)\,| = \sqrt{\frac{A^2+\zeta_b^2B^2}{C^2+\zeta_b^2D^2}} = \left|\frac{B}{D}\right|\sqrt{\frac{\left(\frac{A}{B}\right)^2+\zeta_b^2}{\left(\frac{C}{D}\right)^2+\zeta_b^2}}, \tag{22}$$

where A, B, C, and D is expressed as

$$\begin{aligned} A &= -\beta\,{\eta_b}^2\mu_b-\beta\,{\eta_b}^2\mu_d-\eta^2\mu_d+{\eta_b}^2\mu_b+{\eta_b}^2\mu_d, \\ B &= 2\,\zeta_b\eta\,\eta_b\left(\mu_b+\mu_d\right), \\ C &= \begin{array}{c} -\beta\,\eta^2{\eta_b}^2\mu_b-\beta\,\eta^2{\eta_b}^2\mu_d-\eta^4\mu_b-\eta^4\mu_d+\eta^2{\eta_b}^2\mu_b+\eta^2{\eta_b}^2\mu_d \\ +\beta\,{\eta_b}^2\mu_b+\beta\,{\eta_b}^2\mu_d+\eta^2\mu_b+\eta^2\mu_d-{\eta_b}^2\mu_b-{\eta_b}^2\mu_d+\eta^2 \end{array}, \\ D &= 2\,\zeta_b\eta\,\eta_b\left(\eta-1\right)\left(\eta+1\right)\left(\mu_b+\mu_d\right). \end{aligned} \tag{23}$$

Two constraints are derived from Eq. (22) to obtain optimal frequency and damping ratios [20,23] and express as

$$\left(\frac{A}{B}\right)^2\Big|_\eta = \left(\frac{C}{D}\right)^2\Big|_\eta \quad \text{and} \quad \left(\frac{B}{D}\right)^2\Big|_{\eta_1} = \left(\frac{B}{D}\right)^2\Big|_{\eta_2}. \tag{24}$$

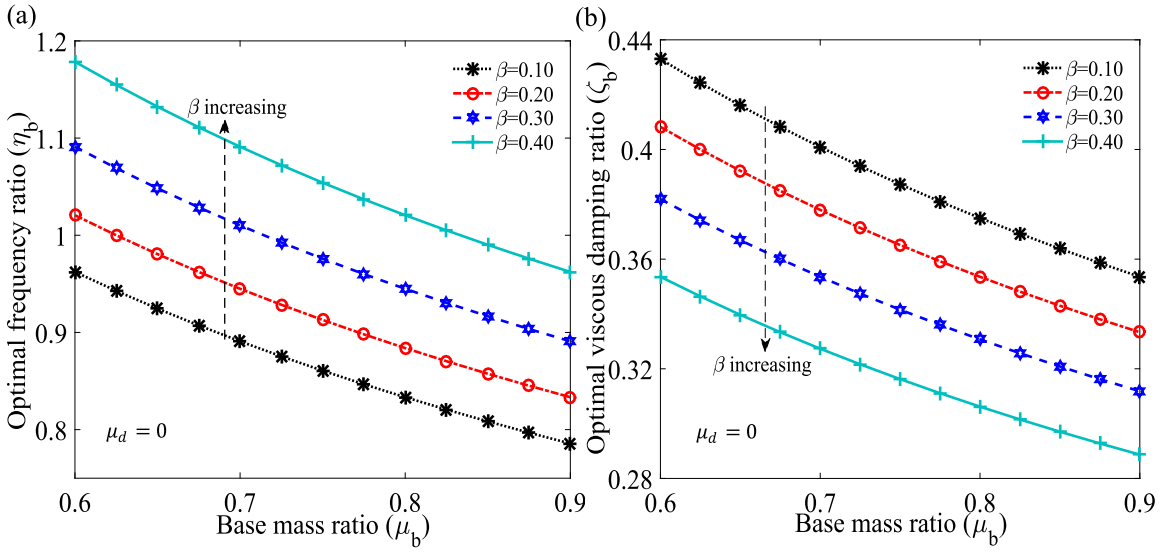

Fig. 4. (a) The differences in optimal frequency ratio η_b versus base mass ratio μ_b for different values of negative stiffness ratio β of NSBI. The black dotted ($\beta = 0.10$), red dash-dotted ($\beta = 0.20$), blue dashed ($\beta = 0.30$), and cyan solid ($\beta = 0.40$) lines with markers are employed to address these plots. (b) The differences in optimal damping ratio ζ_b versus base mass ratio μ_b for different values of negative stiffness ratio β of NSBI. The black dotted ($\beta = 0.10$), red dash-dotted ($\beta = 0.20$), blue dashed ($\beta = 0.30$), and cyan solid ($\beta = 0.40$) lines with markers are employed to address these plots. $\mu_d = 0$ is applied for both graphs.

After applying the first expression of Eq. (24), a equation is determined as [20]

$$\begin{gathered}\left(\mu_b^2+3\,\mu_b\mu_d+2\,\mu_d^2\right)\eta^4\\ +\left(\begin{array}{c}2\,\beta\,\eta_b^2\mu_b^2+4\,\beta\,\eta_b^2\mu_b\mu_d+2\,\beta\,\eta_b^2\mu_d^2-2\,\eta_b^2\mu_b^2-4\,\eta_b^2\mu_b\mu_d\\ -2\,\eta_b^2\mu_d^2-\mu_b^2-3\,\mu_b\mu_d-2\,\mu_d^2-\mu_b-\mu_d\end{array}\right)\eta^2=0.\\ -2\,\beta\,\eta_b^2\mu_b^2-4\,\beta\,\eta_b^2\mu_b\mu_d-2\,\beta\,\eta_b^2\mu_d^2+2\,\eta_b^2\mu_b^2+4\,\eta_b^2\mu_b\mu_d+2\,\eta_b^2\mu_d^2\end{gathered} \tag{25}$$

Using the second constraint of Eq. (24), another equation derives and expresses as

$$\eta_1^2+\eta_2^2=2. \tag{26}$$

Comparing Eqs. (25) and (26), the optimal frequency ratio of is NSIBI derived as

$$(\eta_b)_{\text{opt}}=\sqrt{\frac{1-\mu_b-2\,\mu_d}{2\,\mu_b+2\,\mu_d-2\,\beta\,\mu_b-2\,\beta\,\mu_d}}. \tag{27}$$

$\eta_{1,2}^2$ is derived as

$$(\eta_{1,2})^2=1\pm\sqrt{\frac{2\,\eta_b^2\left(\mu_b+\mu_d\right)(\beta-1)+\mu_b+2\,\mu_d}{\mu_b+2\,\mu_d}}. \tag{28}$$

The optimal $\eta_{1,2}^2$ is derived by substituting Eq. (27) into Eq. (28) and expressed as

$$(\eta_{1,2})_{\text{opt}}^2=1\pm\sqrt{\frac{2\,\mu_b+4\,\mu_d-1}{\mu_b+2\,\mu_d}}. \tag{29}$$

The mathematical expressions for deriving the optimal damping ratio of NSIBI are expressed as

$$\frac{\partial|H_s(\eta)|^2}{\partial\eta^2}|_{\eta_{1,2}^2}=0\quad\text{and}\quad(\zeta_b)_{\text{opt}}=\sqrt{\frac{\zeta_{b1}^2+\zeta_{b2}^2}{2}}. \tag{30}$$

The optimal damping ratio of NSIBI is derived as

$$\begin{gathered}A_1\zeta_b^4+B_1\zeta_b^2+C_1=0\\ \text{and}\quad\zeta_{b1,b2}^2=\frac{-B_1\pm\sqrt{B_1^2-4A_1C_1}}{2A_1},\end{gathered} \tag{31}$$

where A_1, B_1, C_1 are listed in Appendix A. To achieve the optimal damping ratio for NSIBI, Eqs. (27) and (28) are substituted in Eq. (31).

The differences in optimal frequency and damping ratios versus the base mass ratio for different values of negative stiffness ratio of NSIBI are displayed in Figs. 5(a) and 5(b). To obtain Fig. 5, Eqs. (27), (30), and (31) are employed. $\mu_d \neq 0$ is considered for NSIBI. The frequency and damping ratios decrease with the increment of the base mass ratio. In contrast, the frequency ratio increase and the damping ratio decrease with the increment of the negative stiffness ratio. Substituting $\mu_d = 0$ in Eqs. (27), (30), and (31), the exact closed-form expressions for the optimal frequency and damping ratios of NSBI are derived. The differences in optimal frequency and damping ratios versus the base mass ratio for different values of negative stiffness ratio of NSBI are displayed in Figs. 6(a) and 6(b). The frequency and damping ratios decrease with the increment of the base mass ratio. In contrast, the frequency ratio increase, and the damping ratio decrease with the increment of the negative stiffness ratio. H_∞ optimization method is also applied for TBI to derive the optimal design parameters. Therefore, the optimal frequency ratio of TBI is derived as

$$(\nu_b)_{opt}=\sqrt{\frac{1-\mu_b}{2\mu_b}}. \tag{32}$$

The optimal damping ratio of TBI is derived as

$$(\xi_b)_{opt}=\sqrt{\frac{1-\mu_b}{8\,\mu_b}}. \tag{33}$$

The variation of optimal frequency ratio of TBI ν_b versus base mass ratio μ_b is displayed in Fig. 7(a). To acquire Fig. 7(a), Eq. (32) is employed. The optimal frequency ratio of TBI decreases when the base mass ratio increases. The same trend is observed for Fig. 7(b). Therefore, the results imply that a higher base mass ratio enhanced the time period of the isolator and provided additional flexibility at the base of the isolated structure. A higher base mass ratio is recommended for achieving TBI's optimum vibration reduction capacity. The variation of the optimal damping ratio of TBI ξ_b versus base mass ratio μ_b are displayed in Fig. 7(b). To acquire Fig. 7(b), Eq. (33) is employed. TBI's optimal viscous damping ratio decreases when the base mass ratio increases. TBI's optimal viscous damping ratio decreases when the base mass ratio increases. Therefore, the results imply that a higher base mass ratio provides a lower viscous damping ratio of TBI, which is affordable. The higher base mass ratios are recommended for achieving robust performance for H_∞ optimized TBI.

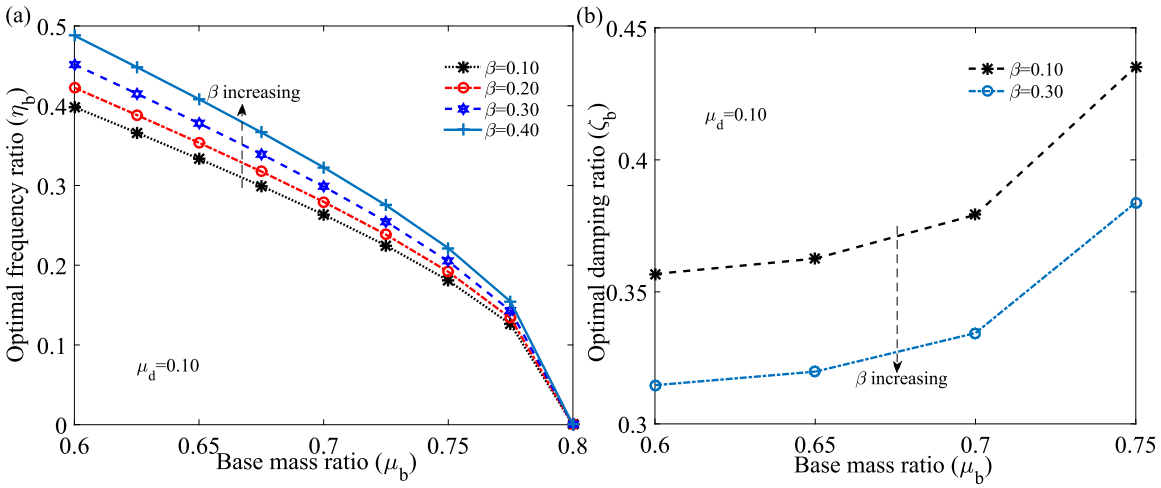

Fig. 5. (a) The differences in optimal frequency ratio η_b versus base mass ratio μ_b for different values of negative stiffness ratio β of NSIBI. The black dotted ($\beta = 0.10$), red dash-dotted ($\beta = 0.20$), blue dashed ($\beta = 0.30$), and sky blue solid ($\beta = 0.40$) lines with markers are employed to address these plots. (b) The differences in optimal damping ratio ζ_b versus base mass ratio μ_b for different values of negative stiffness ratio β of NSIBI. The black dashed ($\beta = 0.10$), and sky blue dash-dotted ($\beta = 0.30$) lines with markers are employed to address these plots. $\mu_d = 0.10$ is applied for both graphs. Eqs. (27), (30), and (31) are employed to obtain both graphs.

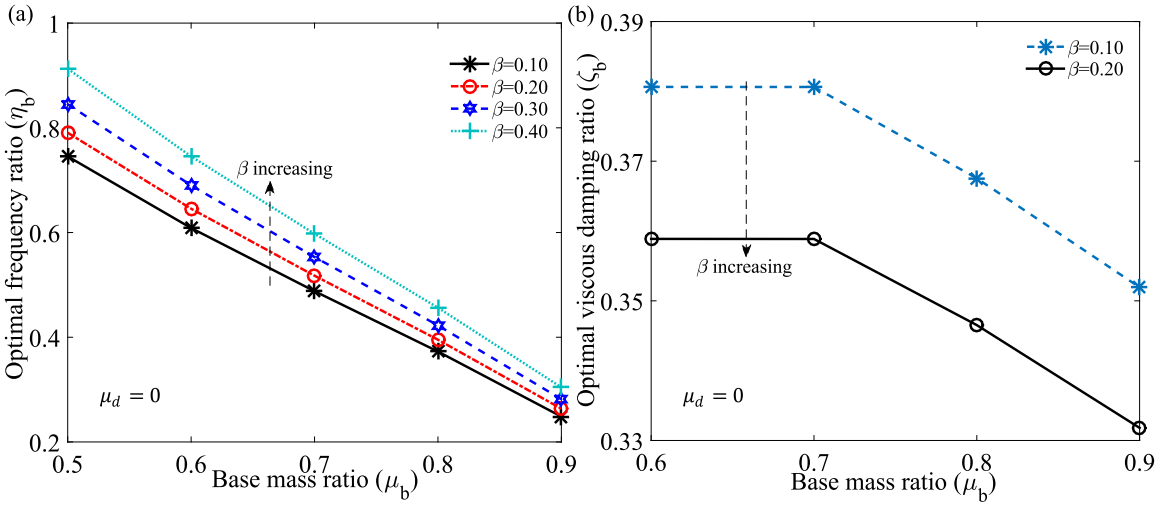

Fig. 6. (a) The differences in optimal frequency ratio η_b versus base mass ratio μ_b for different values of negative stiffness ratio β of NSBI. The black solid ($\beta = 0.10$), red dash-dotted ($\beta = 0.20$), blue dashed ($\beta = 0.30$), and cyan dotted ($\beta = 0.40$) lines with markers are employed to address these plots. (b) The differences in optimal viscous damping ratio ζ_b versus base mass ratio μ_b for different values of negative stiffness ratio β of NSBI. The sky blue dashed ($\beta = 0.10$), and black solid ($\beta = 0.20$) lines with markers are employed to address these plots. $\mu_d = 0$, Eqs. (27), (30), and (31) are employed to obtain both graphs.

5. Robustness of NSIBI and NSBI

The differences in main structural optimal dynamic responses isolated by H_2 optimized NSIBI versus frequency ratio for various damping ratios are displayed in Fig. 8(a). $\mu_b = 0.70$, $\mu_d = 0.10$, $\beta = 0.10$, $\zeta_s = 0$ are considered system parameters. The optimal frequency and damping ratios using Eqs. (16) and (17), i.e., $(\eta_b)_{opt} = 0.7454$ and $(\zeta_b)_{opt} = 0.3248$. $\eta = 0.4433, 1.599$ are the Eigen frequencies at $\zeta_b = 0$. $\eta = 1.313$ is minima point. $\eta = 0.4388, 1.542$ are the resonating frequencies at $(\eta_b)_{opt}$ and $(\zeta_b)_{opt}$. At these frequency regions, the maximum dynamic response mitigation occurs. The anti-resonance frequency region evaluates at $\eta = 2.0$. At $\zeta_b = \infty$, the dynamic response peaks of the isolated structure, i.e., two degrees of freedom systems, are merged into one. The entire system vibrates as a single-degree-of-freedom system (SDOF). The frequency point is evaluated at $\eta = 1.0$.

The differences in H_∞ optimized NSIBI controlled structure's dynamic responses are shown in Fig. 8(b). The system parameters are considered as $\mu_b = 0.70$, $\mu_d = 0.10$, $\beta = 0.10$, $\zeta_s = 0$ and substituting these parameters in Eqs. (27), (30), and (31). Hence, $(\eta_b)_{opt} = 0.2635$ and $(\zeta_b)_{opt} = 0.3792$ are evaluated. $\eta = 0.1643, 1.511$ are the Eigen frequencies at $\zeta_b = 0$. $\eta = 0.7071$ is the anti-resonance frequency. $\eta = 0.1557, 1.506$ are the resonating frequencies; resulting the mitigation of maximum dynamic responses. $\eta = 0.8483$ is the minima frequency point. $\zeta_b = \infty$, the dynamic response peaks of the two degrees of freedom systems are merged into a single-degree-of-freedom system (SDOF). $\eta = 1.0$ is the frequency point. The peak dynamic responses of the main structure isolated by H_2 and H_∞ optimized NSIBI are determined as 3.038 and 2.1538. Therefore, the dynamic response reduction capacity of H_∞ optimized NSIBI is 29.1% superior to H_2 optimized NSIBI.

The variations of main structural optimal dynamic responses isolated by H_2 optimized NSBI for different values of damping ratio are displayed in Fig. 9(a). The system parameters are considered as $\mu_b = 0.70$, $\mu_d = 0$, $\beta = 0.10$, $\zeta_s = 0$. The optimal frequency and damping ratios are determined using Eqs. (16) and (17), i.e., $(\eta_b)_{opt} = 0.8909$ and $(\zeta_b)_{opt} = 0.4009$. $\eta = 0.4966, 1.702$ are the Eigen frequencies at $\zeta_b = 0$. $\eta = 0.4934, 1.697$ are the resonating frequencies at $(\eta_b)_{opt}$ and $(\zeta_b)_{opt}$. At these frequency regions, the maximum dynamic response

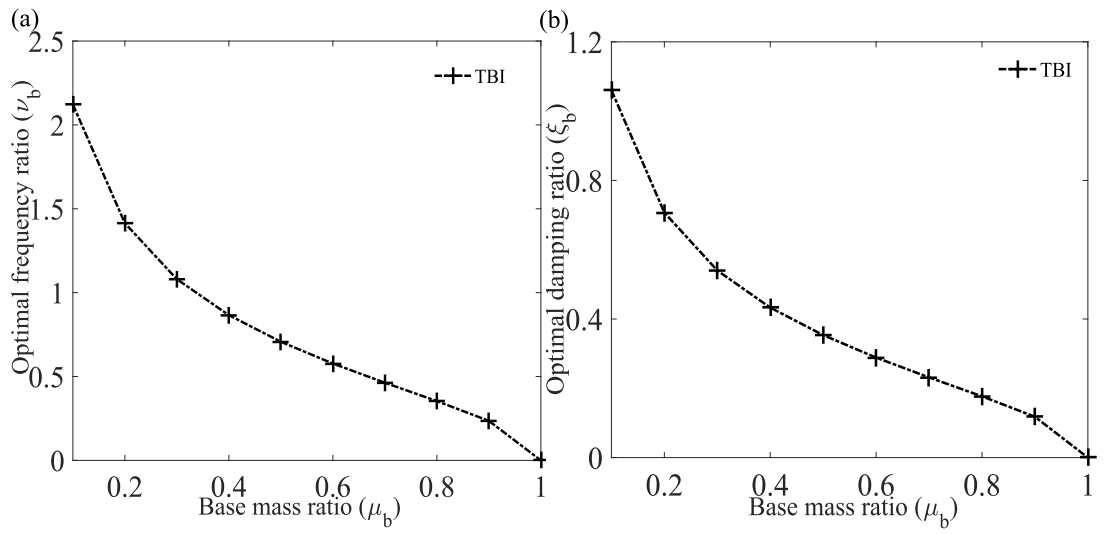

Fig. 7. (a) The variations of optimal frequency ratio of traditional base isolator (TBI) versus base mass ratio. Eq. (32) is employed for this graph. (b) The variation of the optimal viscous ratio of traditional base isolator (TBI) versus base mass ratio. Eq. (33) is employed for this graph. The black dashed line with marker is employed to address both graphs.

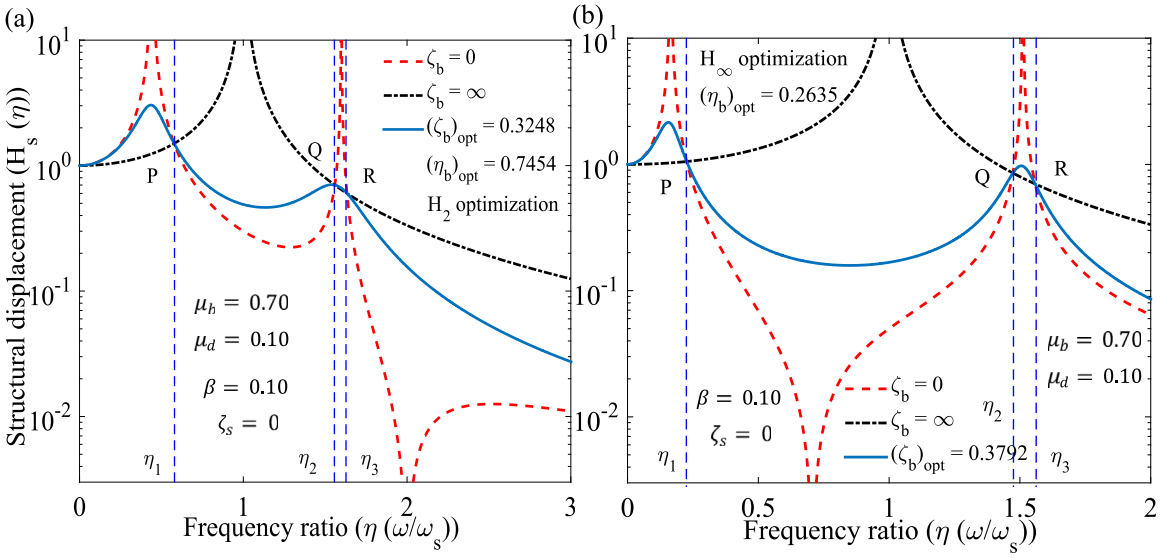

Fig. 8. (a) The differences in main structural optimal dynamic responses isolated by H_2 optimized NSIBI versus frequency ratio for various damping ratios. $\mu_b = 0.70$, $\mu_d = 0.10$, $\beta = 0.10$, $\zeta_s = 0$ are considered system parameters. The optimal frequency and damping ratios are derived using Eqs. (16) and (17), i.e., $(\eta_b)_{opt} = 0.7454$ and $(\zeta_b)_{opt} = 0.3248$. The red dashed ($\zeta_b = 0$), black dash-dotted ($\zeta_b = \infty$), and sky blue solid ($(\zeta_b)_{opt} = 0.3248$) lines are employed to address these plots. (b) The differences in main structural optimal dynamic responses isolated by H_∞ optimized NSIBI versus frequency ratio for various damping ratios. $\mu_b = 0.70$, $\mu_d = 0.10$, $\beta = 0.10$, $\zeta_s = 0$ are considered system parameters. Eqs. (27), (30), and (31) are applied to derive the optimal frequency and damping ratios, i.e., $(\eta_b)_{opt} = 0.2635$ and $(\zeta_b)_{opt} = 0.3792$. The red dashed ($\zeta_b = 0$), black dash-dotted ($\zeta_b = \infty$), and sky blue solid ($(\zeta_b)_{opt} = 0.3792$) lines are employed to address these plots. P, Q, and R indicate the fixed points for both graphs.

mitigation occurs. At $\zeta_b = \infty$, the dynamic response peaks of the isolated structure, i.e., two degrees of freedom systems, are merged into one. The entire system vibrates as a single-degree-of-freedom system (SDOF). The frequency point is evaluated at $\eta = 1.0$.

The variations of H_∞ optimized NSBI controlled structure's dynamic responses are shown in Fig. 9(b). The system parameters are considered as $\mu_b = 0.70$, $\mu_d = 0.0$, $\beta = 0.10$, $\zeta_s = 0$. and substituting these parameters in Eqs. (27), (30), and (31), $(\eta_b)_{opt} = 0.488$ and $(\zeta_b)_{opt} = 0.3806$ are evaluated. $\eta = 0.2894, 1.6$ are the Eigen frequencies at $\zeta_b = 0$. $\eta = 0.2794, 1.597$ are the resonating frequencies, resulting in the mitigation of maximum dynamic responses. $\zeta_b = \infty$, the dynamic response peaks of the two degrees of freedom systems are merged into a single-degree-of-freedom system (SDOF). $\eta = 1.0$ is the frequency point. H_2 and H_∞ optimized NSBI-controlled superstructure's maximum dynamic responses are determined as 2.9858 and 2.4622. Hence, the dynamic response reduction capacity of H_∞ optimized NSBI is 17.53% more than H_2 optimized NSBI.

The differences in the optimal dynamic responses of uncontrolled structures, structures isolated by H_2 optimized NSIBI, NSBI, and traditional base isolator (TBI) versus frequency ratio for various damping ratios are displayed in Fig. 10(a). The system parameters for H_2 optimized isolators and uncontrolled structures are listed in Tables 2 and 3. The values of H_2 and H_∞ optimized system parameters for isolators are listed in Table 2. The system parameters of main structures (uncontrolled and controlled structures) are listed in Table 3. The harmonic excitations are applied at the base of the structures. The peak value of the uncontrolled structure's dynamic response is 10.01. The peak values of dynamic responses of the structures isolated by optimum NSIBI, NSBI, and TBI are determined as 2.96, 2.92, and 5.48. The vibration reduction capacities of H_2 optimized NSIBI and NSBI are

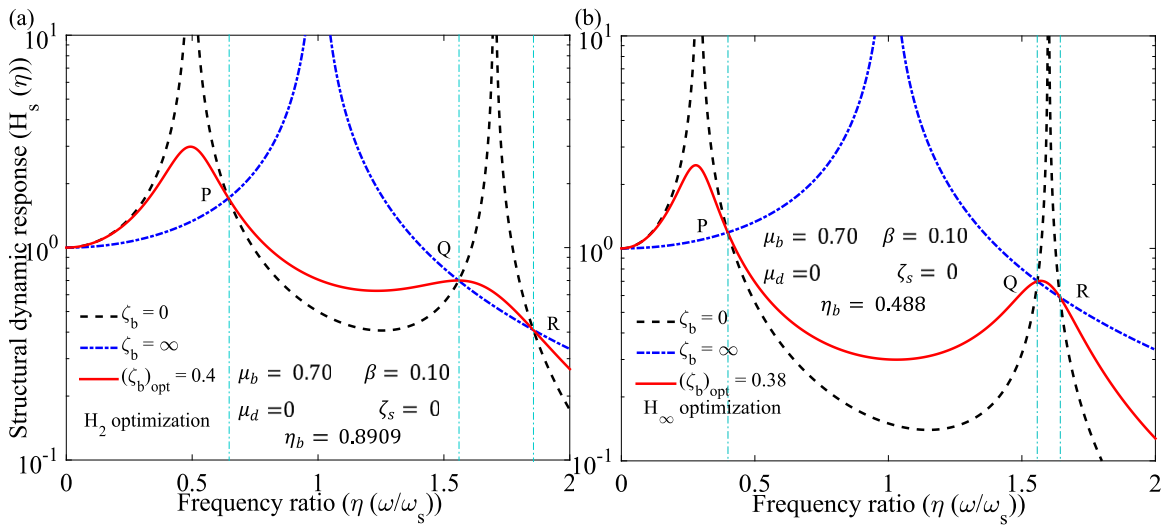

Fig. 9. (a) The differences in main structural optimal dynamic responses isolated by H_2 optimized NSBI versus frequency ratio for various damping ratios. $\mu_b = 0.70$, $\mu_d = 0.0$, $\beta = 0.10$, $\zeta_s = 0$ are considered system parameters. Eqs. (16) and (17) are applied to derive the optimal frequency and damping ratios, i.e., $(\eta_b)_{opt} = 0.8909$ and $(\zeta_b)_{opt} = 0.4009$. The black dashed ($\zeta_b = 0$), blue dash-dotted ($\zeta_b = \infty$), and red solid ($(\zeta_b)_{opt} = 0.4009$) lines are employed to address these plots. (b) The differences in main structural optimal dynamic responses isolated by H_∞ optimized NSBI versus frequency ratio for various damping ratios. $\mu_b = 0.70$, $\mu_d = 0.0$, $\beta = 0.10$, $\zeta_s = 0$ are considered system parameters. Eqs. (27), (30), and (31) are applied to derive the optimal frequency and damping ratios, i.e., $(\eta_b)_{opt} = 0.488$ and $(\zeta_b)_{opt} = 0.38$. The black dashed ($\zeta_b = 0$), blue dash-dotted ($\zeta_b = \infty$), and red solid ($(\zeta_b)_{opt} = 0.38$) lines are employed to address these plots. P, Q, and R indicate the fixed points for both graphs.

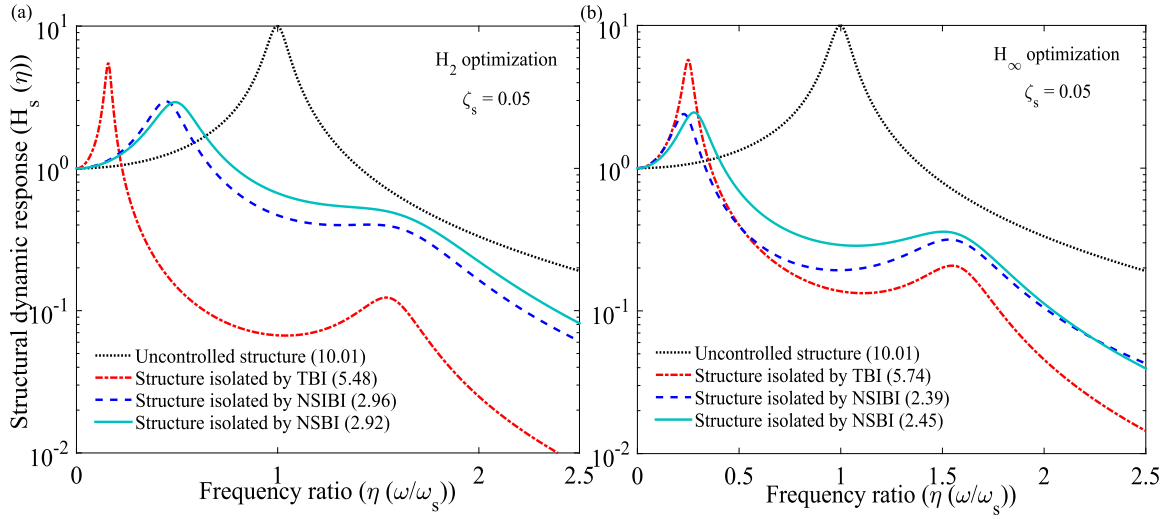

Fig. 10. (a) The differences in the optimal dynamic responses of uncontrolled structures and structures isolated by H_2 optimized NSIBI, NSBI and optimum TBI. The black dotted (uncontrolled), red dash-dotted (structure isolated by TBI), blue dashed (structure isolated by NSIBI), and cyan solid (structure isolated by NSBI) are applied to address each plot. (b) The differences in the optimal dynamic responses of uncontrolled structures and structures isolated by H_∞ optimized NSIBI, NSBI and optimum TBI. The black dotted (uncontrolled), red dash-dotted (structure isolated by TBI), blue dashed (structure isolated by NSIBI), and cyan solid (structure isolated by NSBI) are applied to address each plot. For both graphs, the design parameters are listed in Table 2. $\zeta_s = 0.05$ is considered for both graphs.

Table 2
The values of H_2 and H_∞ optimized system parameters for isolators.

System	Proposed by	H_2 optimization		H_∞ optimization	
		η_b	ζ_b	η_b	ζ_b
NSIBI	This study	0.7968	0.3472	0.3984	0.3567
NSBI	This study	0.8909	0.4009	0.4879	0.3806
TBI	Matsagar and Jangid [48]	0.25	0.15	0.4	0.15

Traditional base isolator (TBI): base mass ratio (μ_B) = 0.70, NSIBI: base mass ratio (μ_b) = 0.60, inerter mass ratio (μ_d = 0.10), NSBI: base mass ratio ($\tilde{\mu}_b$) = 0.70, Mass ratio: $\mu_B = \mu_b + \mu_d = \tilde{\mu}_b$, and negative stiffness ratio $\beta = 0.10$.

significantly 45.98% and 46.71% more than the vibration reduction capacity of TBI.

Table 3
The system parameters of main structures (uncontrolled and controlled structures).

Name	Symbol	Values
Damping ratio	ζ_s	0.05

The differences in the optimal dynamic responses of uncontrolled structures, structures isolated by H_∞ optimized NSIBI, NSBI, and traditional base isolator (TBI) versus frequency ratio for various damping ratios are displayed in Fig. 10(b). The peak value of the uncontrolled structure's dynamic response is 10.01. The peak values of dynamic responses of the structures isolated by optimum NSIBI, NSBI, and TBI are determined as 2.39, 2.45, and 5.74. The vibration reduction

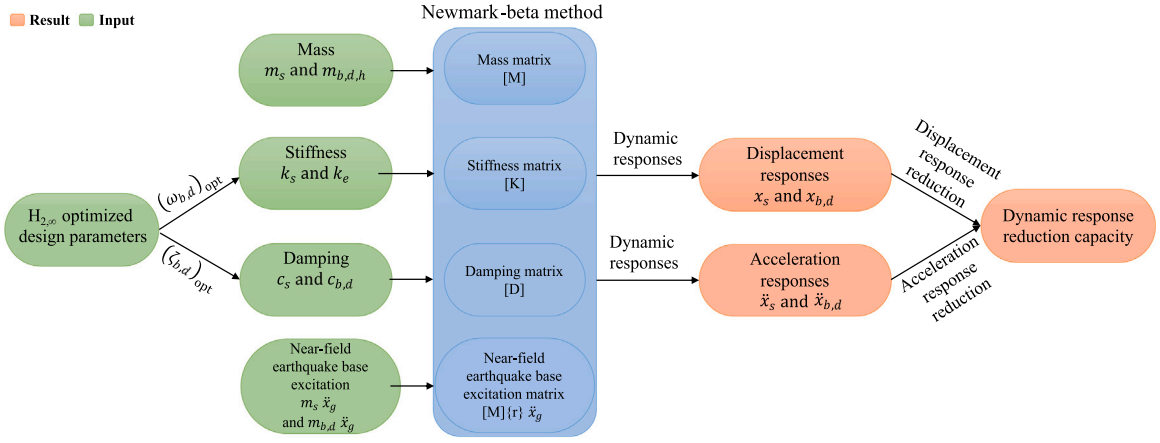

Fig. 11. The algorithm for determining displacement and acceleration response reduction capacities.

Table 4
The system parameters of main structures (uncontrolled and controlled structures).

Name	Symbol	Values
Mass of the structure	m_s	3000 tons
Damping ratio	ζ_s	0.05
Time period of the structure	T_s	0.5 s

Table 5
Details of near-field earthquake records (pulse records) (https://peer.berkeley.edu/peer-strong-ground-motion-databases).

Earthquake	Year	M_w	Recording station	Vs_{30} (m/s)	Component	E_s (km)	PGA,g
Northridge-01	1994	6.7	Rinaldi Receiving Sta	282	NORTHR	10.9	0.87
Chi-Chi, Taiwan	1999	7.6	TCU065	306	CHICHI	26.7	0.82

capacities of H_∞ optimized NSIBI and NSBI are significantly 58.36% and 57.32% more than the vibration reduction capacity of TBI.

Newmark-beta method is applied to determine the time domain responses of the isolated structures subjected to near-field earthquake records with pulses. In addition, the efficiency of the optimal closed-form solutions for the proposed systems is also cross-checked through this time domain analysis. The dynamic response reduction capacities of the proposed dampers in the time domain, such as displacement and acceleration response reduction capacities, are determined using the Newmark-beta method. The algorithm for this study is introduced in Fig. 11. MATLAB environment utilizes to perform this numerical study. The main structure is an uncontrolled structure, and the uncontrolled structure is a single degree of freedom (SDOF) system with the mass of the structure m_s = 3000 tons, damping ratio ζ_s = 0.05, and time period of the structure T_s = 0.5 s The uncontrolled structures with the same system parameters are mounted on a conventional isolation base, i.e., traditional base isolator (TBI), NSIBI, and NSBI. For the conventional isolation base, the base damping ratio considers as 15% in order to have an equal comparison basis with the proposed isolation systems, i.e., NSIBI and NSBI. The system parameters of the main structures are listed in Table 4. The near-field earthquake records are downloaded from the Pacific Earthquake Engineering Research Center (https://peer.berkeley.edu/peer-strong-ground-motion-databases). The detailed properties of near-field earthquake records are listed in Table 5. The response spectra of the considered earthquake records are shown in Fig. 12 with 5% damping. Near-field earthquakes are more dangerous than far-field earthquakes [19]. Hence, the numerical study is continued with near-field earthquake records (pulse records). The

Table 6
The values of H_2 and H_∞ optimized system parameters for isolators.

System	Proposed by	H_2 optimization		H_∞ optimization	
		η_b	ζ_b	η_b	ζ_b
NSIBI	This study	0.7968	0.3472	0.3984	0.3567
NSBI	This study	0.8909	0.4009	0.4879	0.3806
TBI	Chowdhury and Banerjee (H_2) [49]	0.8452	0.4226	...	...
TBI	This study (Eq. (32) and Eq. (33)) (H_∞)	...	...	0.4629	0.2315

Traditional base isolator (TBI): base mass ratio (μ_B) = 0.70, NSIBI: base mass ratio (μ_b) = 0.60, inerter mass ratio (μ_d = 0.10), NSBI: base mass ratio ($\tilde{\mu}_b$) = 0.70, Mass ratio: $\mu_B = \mu_b + \mu_d = \tilde{\mu}_b$, and negative stiffness ratio $\beta = 0.10$.

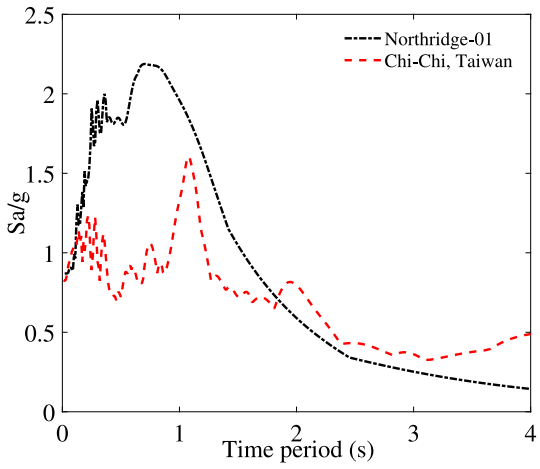

Fig. 12. Response spectra of earthquake base excitations. The black dash-dotted (Northridge-01) and red dash (Chi-Chi, Taiwan) lines are applied to address these plots. 5% damping is considered to determine this graph.

values of H_2 and H_∞ optimized system parameters for each isolator are listed in Table 6.

The differences in the optimal displacement of the main structure isolated by H_2 optimized NSBI, NSIBI, and TBI subjected to Northridge-01 base excitation are shown in Fig. 13(a). The maximum displacements of the uncontrolled structure and structures isolated by H_2 optimized TBI, NSIBI, and NSBI are determined as 0.0116 m, 0.0097 m, 0.0086 m, and 0.007 m. Therefore, the dynamic response reduction capacities of H_2 optimized NSIBI and NSBI are significantly 11.34% and 27.83% superior to H_2 optimized TBI. The differences in the optimal displacement of the main structure isolated by H_∞ optimized NSBI, NSIBI, and TBI subjected to Northridge-01 base excitation are shown in Fig. 13(b). The maximum displacements of the uncontrolled

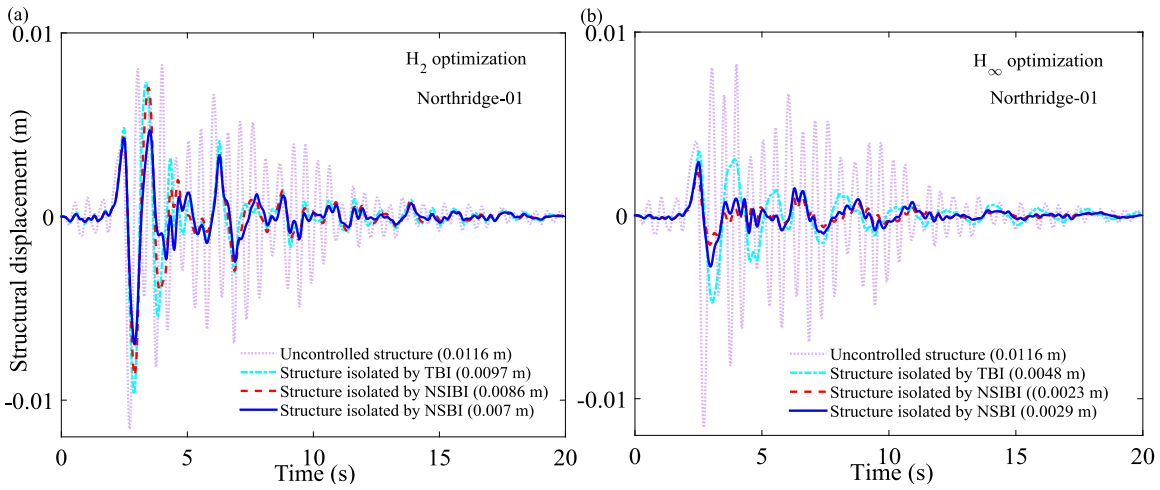

Fig. 13. (a) The differences in the optimal displacement of the main structure isolated by H_2 optimized NSBI, NSIBI, and optimum TBI [49] subjected to Northridge-01 base excitation. (b) The differences in the optimal displacement of the main structure isolated by H_∞ optimized NSBI, NSIBI, and optimum TBI (Eqs. (32) and (33)) subjected to Northridge-01 base excitation. For both graphs, the design parameters are listed in Table 6. Pink dotted (uncontrolled structure), cyan dash-dotted (structure isolated by TBI), red dashed (structure isolated by NSIBI), and blue solid (structure isolated by NSBI) lines are employed to address each plot for both graphs.

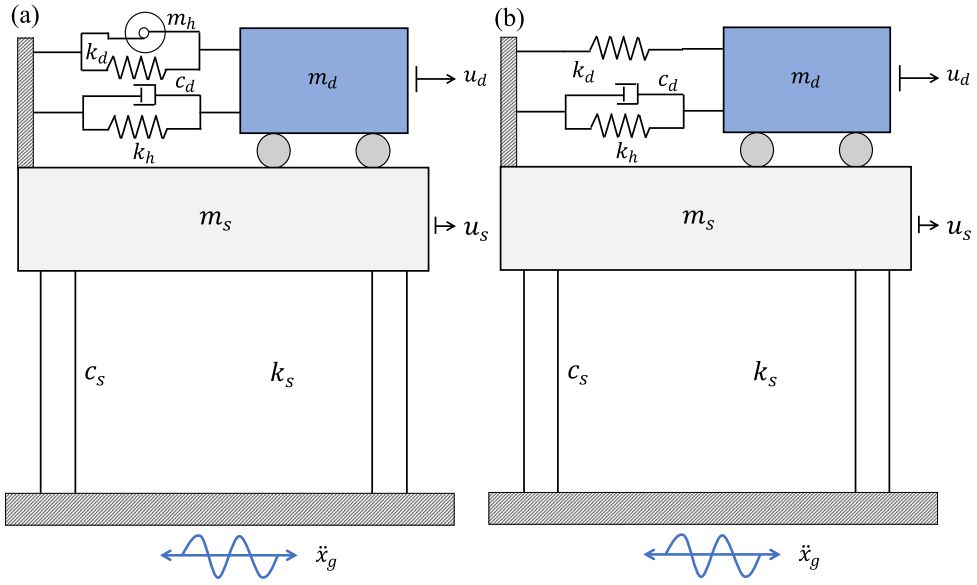

Fig. 14. SDOF systems controlled by (a) NSITMD and (b) NSTMD subjected to base excitation.

Table 7
The values of inerter masses for NSITMD and NSTMD.

Mass	NSITMD	NSTMD
m_h	$m_h \neq 0$	$m_h = 0$

structure and structures isolated by H_∞ optimized TBI, NSIBI, and NSBI are determined as 0.0116 m, 0.0048 m, 0.0023 m, and 0.0029 m. Therefore, the dynamic response reduction capacities of H_∞ optimized NSIBI and NSBI are significantly 52.08% and 39.58% superior to H_∞ optimized TBI.

6. Novel tuned mass dampers

The structural diagrams of SDOF systems controlled by novel TMD display in Figs. 14(a) and 14(b). m_d, k_d, and c_d define the mass, stiffness, and damping of novel TMD. m_h defines the inerter mass. k_h defines the negative stiffness of the novel TMD, i.e., $k_h = \alpha k_d$. Considering $m_h = 0$ for NSITMD, NSTMD is mathematically formulated. The values of inerter masses for NSITMD and NSTMD are listed in Table 7. m_s, k_s, and c_s define the mass, stiffness, and damping of SDOF systems. $\ddot{x}_g$ defines the base excitation. u_s and u_d define the absolute dynamic response of SDOF systems and novel TMD. Newton's second law applies to derive the governing equations of motion of the SDOF systems controlled by the novel TMD, such as NSITMD and NSTMD subjected to base excitation and expressed as

$$\begin{aligned} m_s\ddot{x}_s + k_s x_s + c_s\dot{x}_s - m_h\ddot{x}_d - c_d\dot{x}_d - k_e x_d &= -m_s\ddot{x}_g, \\ m_d\ddot{x}_d + m_d\ddot{x}_s + m_h\ddot{x}_d + c_d\dot{x}_d + k_e x_d &= -m_d\ddot{x}_g, \end{aligned} \tag{34}$$

where $k_e = k_d - k_h$ defines the effective stiffness of NSITMD. $c_s = 2\,m_s\zeta_s\omega_s$ and $k_s = m_s\omega_s^2$ are the damping and stiffness of the SDOF systems. $c_d = 2\zeta_d(m_h + m_d)\omega_d$ and $k_d = (m_h + m_d)\omega_d^2$ are the damping and stiffness of NSITMD. $x_s = u_s - x_g$, $x_d = u_d - u_s$ define the relative dynamic responses of the primary structure and the novel damper. The controlled structure is subjected to harmonic excitation. $x_s = X_s e^{i\omega t}$, $x_d = X_d e^{i\omega t}$, and $\ddot{x}_g = A_g e^{i\omega t}$ are the steady state solutions which are

substituted in Eq. (34). Hence, the transfer function is derived as

$$\begin{bmatrix} 2q\zeta_s\omega_s + q^2 + {\omega_s}^2 & A_{12} \\ q^2\mu_d & A_{22} \end{bmatrix} \begin{Bmatrix} X_s \\ X_d \end{Bmatrix} = -\begin{bmatrix} 1 \\ \mu_d \end{bmatrix} A_g,$$
$$A_{12} = -q^2\mu_h - 2q\zeta_d\left(\mu_d+\mu_h\right)\omega_d - \left(\mu_d+\mu_h\right){\omega_d}^2 + \alpha\left(\mu_d+\mu_h\right){\omega_d}^2,$$
$$A_{22} = q^2\mu_d + q^2\mu_h + 2q\zeta_d\left(\mu_d+\mu_h\right)\omega_d + \left(\mu_d+\mu_h\right){\omega_d}^2 - \alpha\left(\mu_d+\mu_h\right){\omega_d}^2, \tag{35}$$

where $\alpha = k_h/k_d$ defines the negative stiffness ratio of the novel TMD. The dynamic responses of the SDOF system and NSITMD determine as

$$H_s(q) = \frac{X_s}{A_g} = \frac{\begin{matrix} -\alpha\,{\mu_d}^2{\omega_d}^2 - \alpha\,\mu_d\mu_h{\omega_d}^2 + 2q\zeta_d{\mu_d}^2\omega_d + 2q\zeta_d\mu_d\mu_h\omega_d \\ -\alpha\,{\omega_d}^2\mu_d - \alpha\,{\omega_d}^2\mu_h + q^2\mu_d\mu_h + 2q\zeta_d\omega_d\mu_d + 2q\zeta_d\omega_d\mu_h \\ +{\mu_d}^2{\omega_d}^2 + \mu_d\mu_h{\omega_d}^2 + q^2\mu_d + q^2\mu_h + {\omega_d}^2\mu_d + {\omega_d}^2\mu_h \end{matrix}}{\Delta}, \tag{36}$$

$$H_d(q) = \frac{X_d}{A_g} = \frac{\omega_s\mu_d\left(2q\zeta_s + \omega_s\right)}{\Delta}. \tag{37}$$

The denominator (Δ) of the dynamic response function is separated into its real and imaginary parts as obtains as

$$\begin{matrix} \Delta = & \alpha\,q^2{\mu_d}^2{\omega_d}^2 + \alpha\,q^2\mu_d\mu_h{\omega_d}^2 + 2\alpha\,q\zeta_s\mu_d{\omega_d}^2\omega_s + 2\alpha\,q\zeta_s\mu_h{\omega_d}^2\omega_s - 2q^3\zeta_d{\mu_d}^2\omega_d \\ & -2q^3\zeta_d\mu_d\mu_h\omega_d - 4q^2\zeta_d\zeta_s\mu_d\omega_d\omega_s - 4q^2\zeta_d\zeta_s\mu_h\omega_d\omega_s + \alpha\,q^2\mu_d{\omega_d}^2 + \alpha\,q^2\mu_h{\omega_d}^2 \\ & +\alpha\,\mu_d{\omega_d}^2{\omega_s}^2 + \alpha\,\mu_h{\omega_d}^2{\omega_s}^2 - q^4\mu_d\mu_h - 2q^3\zeta_d\mu_d\omega_d - 2q^3\zeta_d\mu_h\omega_d - q^2{\mu_d}^2{\omega_d}^2 \\ & -2q^3\zeta_s\mu_d\omega_s - 2q^3\zeta_s\mu_h\omega_s - q^2\mu_d\mu_h{\omega_d}^2 - 2q\zeta_d\mu_d\omega_d{\omega_s}^2 - 2q\zeta_d\mu_h\omega_d{\omega_s}^2 \\ & -2q\zeta_s\mu_d{\omega_d}^2\omega_s - 2q\zeta_s\mu_h{\omega_d}^2\omega_s - q^4\mu_d - q^4\mu_h - q^2\mu_d{\omega_d}^2 - q^2\mu_d{\omega_s}^2 \\ & -q^2\mu_h{\omega_d}^2 - q^2\mu_h{\omega_s}^2 - \mu_d{\omega_d}^2{\omega_s}^2 - \mu_h{\omega_d}^2{\omega_s}^2. \end{matrix} \tag{38}$$

The total effective mass of NSITMD obtains as $m_e = m_d + m_h$. Accordingly, the effective mass and stiffness ratios derive as

$$\mu_e = \frac{m_d + m_h}{m_s} = \mu_d + \mu_h. \tag{39}$$

The total effective stiffness of NSITMD is derived as

$$k_e = k_d - k_h = k_d(1-\alpha). \tag{40}$$

The effective stiffness ratio is derived as

$$\kappa_e = \frac{k_d - k_h}{k_d} = \frac{\left(\mu_d+\mu_h\right)(1-\alpha)}{\mu_d}. \tag{41}$$

The contour diagram of effective mass as a function of inerter and damper mass ratios is displayed in Fig. 15(a). To determine this graph, Eq. (39) applies for this graph. The effective mass ratio increases as the damper and inerter mass ratios increase. The contour diagram of effective stiffness as a function of inerter and damper mass ratios is displayed in Fig. 15(b). To obtain this graph, Eq. (41) is applied. The effective stiffness ratio increases as the damper and inerter mass ratios increase. The total effective stiffness of the negative stiffness tuned mass damper is derived as

$$k_e = k_d - k_h = k_d(1-\alpha), \tag{42}$$

where $k_h = \alpha k_d$ refers to the stiffness ratio of the negative stiffness device to the novel damper. The effective stiffness ratio is derived as

$$\kappa_e = \frac{k_d - k_h}{k_d} = (1-\alpha). \tag{43}$$

The difference in the effective stiffness ratio versus the negative stiffness ratio of NSTMD is shown in Fig. 16. The effective stiffness decreases as the negative stiffness ratio of NSTMD increases. A higher stiffness ratio provides a more flexible base for the controlled structures, increasing the NSTMD's dynamic response reduction capacity.

7. H_2 optimization for NSITMD and NSTMD

H_2 optimization employs to derive the optimal design parameters for NSITMD and NSTMD subjected to random-white noise excitation [19,20]. $\zeta_s = 0$ considers to perform this optimization. The SD of the main structure derives using Eqs. (9), (36) and (38) and expressed as

$$\sigma^2_{x_s} = \frac{S_0\pi\left(\begin{matrix} \left(\mu_d+1\right)^4\left(\mu_d+\mu_h\right)^2(\alpha-1)^2{\omega_d}^4 + \left(\left(\mu_h+1\right)\mu_d+\mu_h\right)^2{\omega_s}^4 \\ -\left(\mu_d+\mu_h\right)\left(\mu_d+1\right)^2{\omega_s}^2\left(\begin{matrix}\left(-4{\zeta_d}^2+\alpha-1\right)\mu_d{}^2 \\ -2\left(\mu_h+1\right)\left(2{\zeta_d}^2+\alpha-1\right)\mu_d \\ -2\mu_h\left(2{\zeta_d}^2+\alpha-1\right)\end{matrix}\right){\omega_d}^2 \end{matrix}\right)}{2\omega_d\zeta_d\left(\mu_d+\mu_h\right){\mu_d}^2{\omega_s}^6}. \tag{44}$$

The damping ratio and frequency of the NSITMD are derived by partially differentiating Eq. (44). The mathematical formulations are expressed as

$$\frac{\partial\sigma^2_{x_s}}{\partial\zeta_d} = 0 \quad \text{and} \quad \frac{\partial\sigma^2_{x_s}}{\partial\omega_d} = 0. \tag{45}$$

The damping ratio of NSITMD is derived by substituting Eq. (44) into the first equation of Eq. (45). Hence, the damping ratio of NSITMD is derived as

$$\zeta_d = \sqrt{\frac{\left(\mu_d+1\right)^4\left(\mu_d+\mu_h\right)^2(\alpha-1)^2{\omega_d}^4 + {\omega_s}^4\left(\left(\mu_h+1\right)\mu_d+\mu_h\right)^2 - (\alpha-1)\left(\mu_d+\mu_h\right){\omega_s}^2\left({\mu_d}^2+\left(-2\mu_h-2\right)\mu_d-2\mu_h\right)\left(\mu_d+1\right)^2{\omega_d}^2}{4\,{\omega_d}^2{\omega_s}^2\left(\mu_d+1\right)^3\left(\mu_d+\mu_h\right)^2}}. \tag{46}$$

The SD is modified by substituting Eq. (46) into Eq. (44) and expressed as (seeBox I.) The natural frequency of NSITMD is derived by substituting Eq. (47) into the second expression of Eq. (45) and expressed as

$$(\omega_d)_{opt} = \sqrt{\frac{{\mu_d}^2{\omega_s}^2 - 2\mu_d\mu_h{\omega_s}^2 - 2\mu_d{\omega_s}^2 - 2\mu_h{\omega_s}^2}{\begin{matrix}2\alpha\,{\mu_d}^3 + 2\alpha\,{\mu_d}^2\mu_h + 4\alpha\,{\mu_d}^2 + 4\alpha\,\mu_d\mu_h - 2{\mu_d}^3 - 2{\mu_d}^2\mu_h \\ +2\alpha\,\mu_d + 2\alpha\,\mu_h - 4{\mu_d}^2 - 4\mu_d\mu_h - 2\mu_d - 2\mu_h\end{matrix}}}. \tag{48}$$

The non-dimensional form of Eq. (48) is derived as

$$(\eta_d)_{opt} = \sqrt{\frac{{\mu_d}^2 - 2\mu_d\mu_h - 2\mu_d - 2\mu_h}{\begin{matrix}2\alpha\,{\mu_d}^3 + 2\alpha\,{\mu_d}^2\mu_h + 4\alpha\,{\mu_d}^2 + 4\alpha\,\mu_d\mu_h - 2{\mu_d}^3 - 2{\mu_d}^2\mu_h \\ +2\alpha\,\mu_d + 2\alpha\,\mu_h - 4{\mu_d}^2 - 4\mu_d\mu_h - 2\mu_d - 2\mu_h\end{matrix}}}. \tag{49}$$

The damping ratio of NSITMD is derived by substituting Eq. (48) into Eq. (46). Hence, the optimal damping ratio is derived as

$$(\zeta_d)_{opt} = \sqrt{\frac{\left({\mu_d}^2 + \left(-4\mu_h-4\right)\mu_d - 4\mu_h\right){\mu_d}^2(1-\alpha)}{8\left(\mu_d+1\right)\left(\mu_d+\mu_h\right)\left({\mu_d}^2+\left(-2\mu_h-2\right)\mu_d-2\mu_h\right)}}. \tag{50}$$

The differences in optimal frequency and damping ratios versus the damper mass ratio for different values of negative stiffness ratio of NSITMD are displayed in Figs. 17(a) and 17(b). To obtain Fig. 17, Eqs. (49) and (50) are employed. $\mu_h \neq 0$ is considered for NSITMD. The frequency and damping ratios decrease with the increment of the damper mass ratio. In contrast, the frequency ratio increase and the damping ratio decrease with the increment of the negative stiffness ratio. Substituting $\mu_h = 0$ in Eqs. (49) and (50), the exact closed-form expressions for the optimal frequency and damping ratios of NSTMD are derived.

The differences in optimal frequency and damping ratios versus the damper mass ratio for different values of negative stiffness ratio

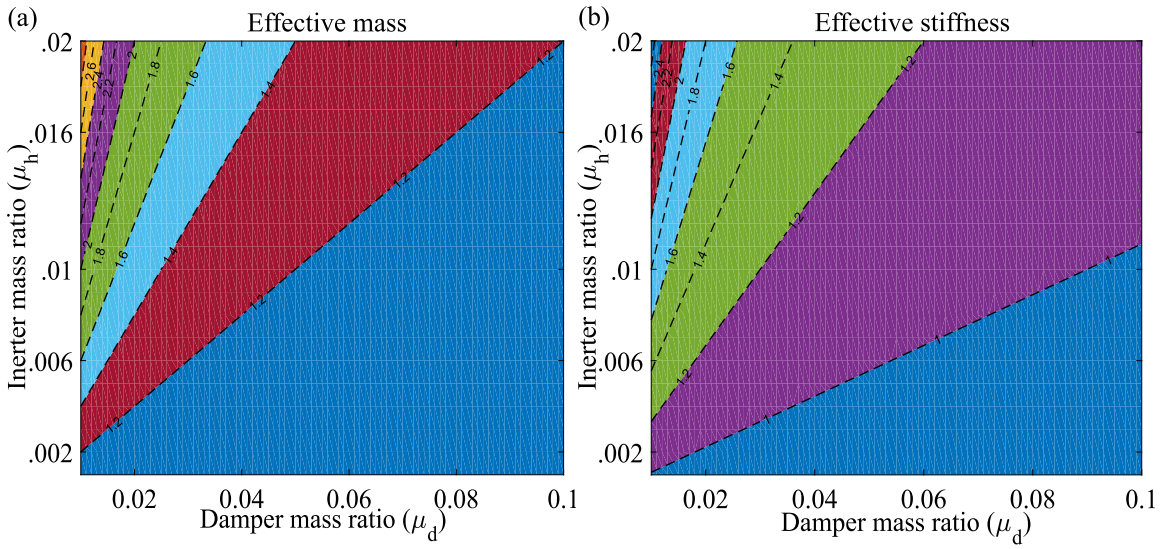

Fig. 15. The contour diagrams of (a) effective mass and (b) effective stiffness as a function of inerter mass ratio and damper mass ratio.

$$\sigma_{x_s}^2 = \frac{2S_0\pi\left(\begin{array}{c}(\mu_d+1)^4(\mu_d+\mu_h)^2(\alpha-1)^2{\omega_d}^4+((\mu_h+1)\mu_d+\mu_h)^2{\omega_s}^4\\-(\mu_d+1)^2(\alpha-1)(\mu_d+\mu_h)(\mu_d{}^2+(-2\mu_h-2)\mu_d-2\mu_h){\omega_s}^2{\omega_d}^2\end{array}\right)}{\omega_d(\mu_d+\mu_h)\mu_d{}^2{\omega_s}^6\sqrt{\dfrac{(\mu_d+1)^4(\mu_d+\mu_h)^2(\alpha-1)^2{\omega_d}^4+{\omega_s}^4((\mu_h+1)\mu_d+\mu_h)^2}{-(\alpha-1){\omega_s}^2(\mu_d+\mu_h)(\mu_d{}^2+(-2\mu_h-2)\mu_d-2\mu_h)(\mu_d+1)^2{\omega_d}^2}}{\omega_d{}^2\omega_s{}^2(\mu_d+1)^3(\mu_d+\mu_h)^2}}}. \tag{47}$$

Box I.

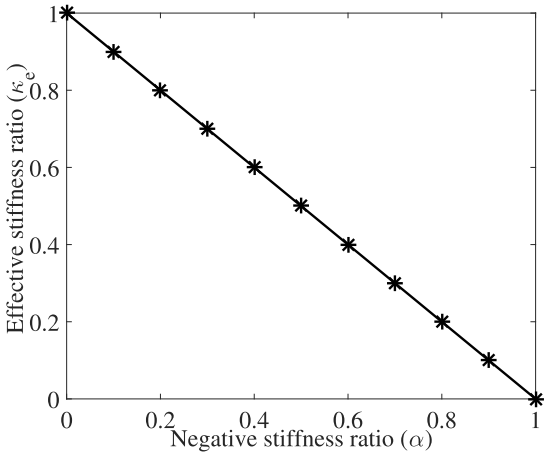

Fig. 16. The difference in effective stiffness ratio versus negative stiffness ratio of NSTMD.

of NSTMD are displayed in Figs. 18(a) and 18(b). The frequency and damping ratios decrease with the increment of the damper mass ratio. The frequency ratio increase and the damping ratio decrease with the increment of the negative stiffness ratio. In addition, the tendency of Figs. 17 and 18 are same. As the in-build negative stiffness of the core material of the NSITMD and NSTMD affects the optimal frequency and damping ratios of NSITMD and NSTMD.

Precisely, to distinguish the effect of inerters on the optimal frequency parameters of the NSITMD and NSTMD, The differences in optimal frequency ratio η_d versus damper mass ratio μ_d for different values of inerter mass ratio μ_h of novel tuned mass dampers are shown in Fig. 19(a). The optimal frequency ratio increases as the inerter mass ratio increases; accordingly, the tuning ratio of NSITMD is more than the NSTMD. Besides, the effects of inerters on the damping of the novel dampers are determined. The differences in optimal damping ratio ζ_d versus damper mass ratio μ_d for different values of inerter mass ratio μ_h of novel tuned mass dampers are shown in Fig. 19(b). The damping ratio of the novel dampers decreases as the inerter mass ratio increases. Hence, the damping of the NSITMD is less than that of NSTMD, which is affordable. Therefore, a moderate inerter mass ratio is recommended to achieve robust vibration reduction for NSITMD and NSTMD with an affordable range.

8. H_∞ optimization for NSITMD and NSTMD

H_∞ optimization is employed to derive the optimal design parameters for NSITMD and NSTMD subjected to harmonic excitation [20]. $\zeta_s = 0$ considers to perform this optimization. The transfer function in Eq. (35) is transformed into a non-dimensional manner. Therefore, the non-dimensional transfer function is derived as

$$\begin{bmatrix} -\eta^2+1+2i\eta\zeta_s & A_{12} \\ -\eta^2\mu_d & A_{22}\end{bmatrix}\begin{Bmatrix} X_s \\ X_d\end{Bmatrix} = -\begin{bmatrix} 1 \\ \mu_d\end{bmatrix}\frac{A_g}{\omega_s^2},$$
$$A_{12} = \eta^2\mu_h - 2i\eta\zeta_d(\mu_d+\mu_h)\eta_d - (\mu_d+\mu_h)\eta_d{}^2+\alpha(\mu_d+\mu_h)\eta_d{}^2,$$
$$A_{22} = -\eta^2\mu_d-\eta^2\mu_h+2i\eta\zeta_d(\mu_d+\mu_h)\eta_d+(\mu_d+\mu_h)\eta_d{}^2-\alpha(\mu_d+\mu_h)\eta_d{}^2. \tag{51}$$

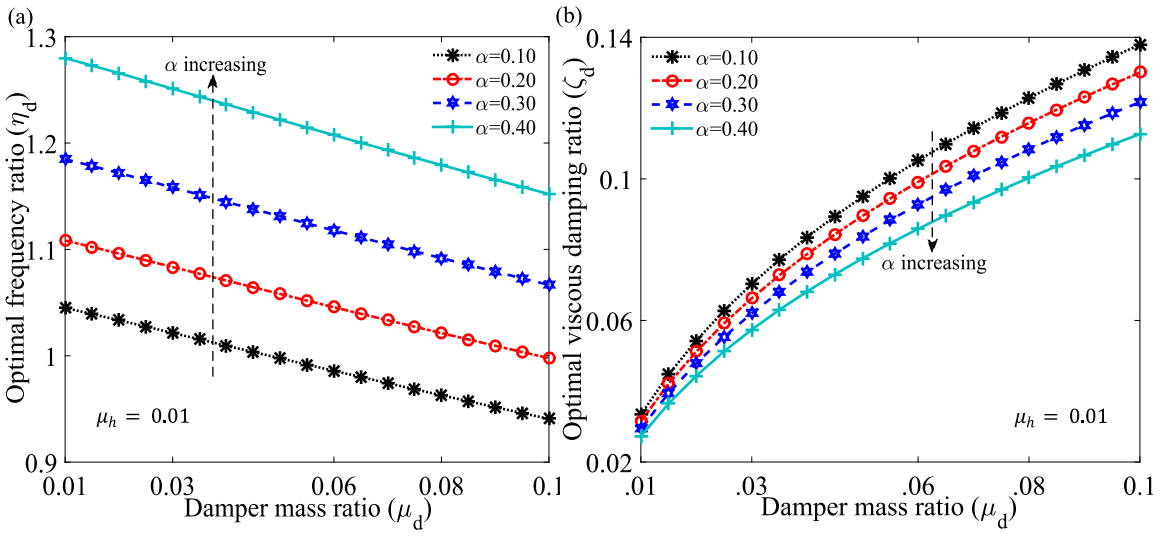

Fig. 17. (a) The differences in optimal frequency ratio η_d versus damper mass ratio μ_d for different values of negative stiffness ratio α of NSITMD. The black solid ($\alpha = 0.10$), red dash-dotted ($\alpha = 0.20$), blue dashed ($\alpha = 0.30$), and cyan dotted ($\alpha = 0.40$) lines with markers are employed to address these plots. (b) The differences in optimal viscous damping ratio ζ_d versus damper mass ratio μ_d for different values of negative stiffness ratio α of NSITMD. The black solid ($\alpha = 0.10$), red dash-dotted ($\alpha = 0.20$), blue dashed ($\alpha = 0.30$), and cyan dotted ($\alpha = 0.40$) lines with markers are employed to address these plots. $\mu_h = 0.01$ is applied for both graphs. Eqs. (49) and (50) are employed to obtain both graphs.

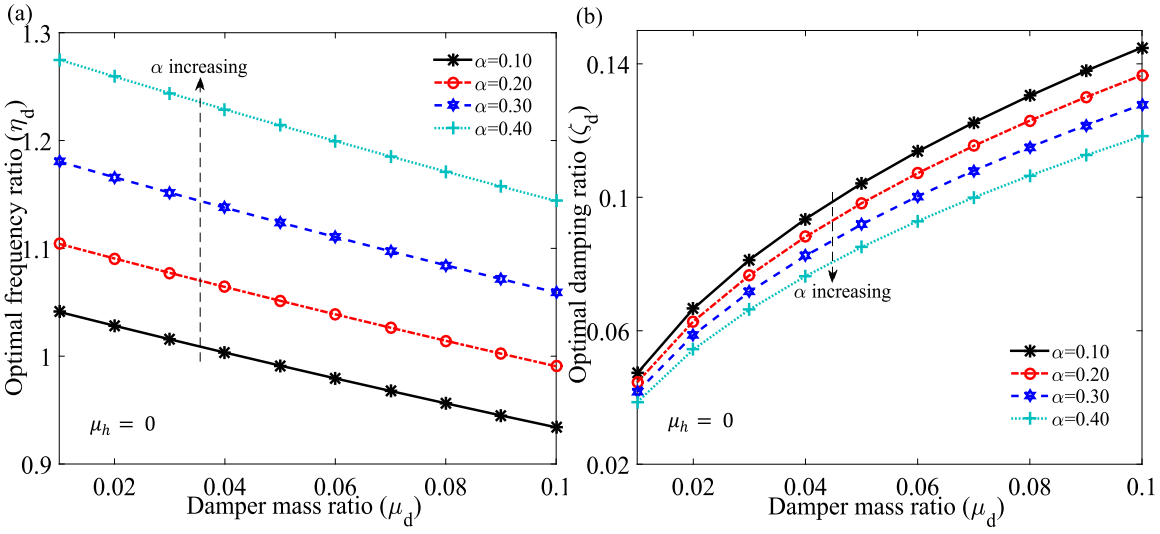

Fig. 18. (a) The differences in optimal frequency ratio η_d versus damper mass ratio μ_d for different values of negative stiffness ratio α of NSTMD. The black solid ($\alpha = 0.10$), red dash-dotted ($\alpha = 0.20$), blue dashed ($\alpha = 0.30$), and cyan dotted ($\alpha = 0.40$) lines with markers are employed to address these plots. (b) The differences in optimal viscous damping ratio ζ_d versus damper mass ratio μ_d for different values of negative stiffness ratio α of NSTMD. The black solid ($\alpha = 0.10$), red dash-dotted ($\alpha = 0.20$), blue dashed ($\alpha = 0.30$), and cyan dotted ($\alpha = 0.40$) lines with markers are employed to address these plots. $\mu_h = 0$ is applied for both graphs. Substituting $\mu_h = 0$ in Eqs. (49) and (50), the exact closed-form expressions for the optimal frequency and damping ratios of NSTMD are derived and applied to obtain both graphs.

The dynamic response of the primary structure is derived as

$$H_s(\eta) = \frac{X_s}{A_g}\omega_s^2 = \frac{\begin{array}{c}-\alpha\,\eta_d{}^2\mu_d{}^2 - \alpha\,\eta_d{}^2\mu_d\mu_h - \alpha\,\eta_d{}^2\mu_d - \alpha\,\eta_d{}^2\mu_h - \eta^2\mu_d\mu_h \\ +\eta_d{}^2\mu_d{}^2 + \eta_d{}^2\mu_d\mu_h - \eta^2\mu_d - \eta^2\mu_h + \eta_d{}^2\mu_d + \eta_d{}^2\mu_h \\ +2i\eta_d\eta\,\zeta_d\,(\mu_d+1)\,(\mu_d+\mu_h)\end{array}}{\Delta}. \tag{52}$$

The dynamic response NSITMD is derived as

$$H_d(\eta) = \frac{X_d}{A_g}\omega_s^2 = \frac{\mu_d\,(2i\eta\,\zeta_s+1)}{\Delta}. \tag{53}$$

The denominator (Δ) of the dynamic response function is separated into its real and imaginary parts as obtains as

$$\Delta = \begin{array}{c}-\alpha\,\eta^2\eta_d{}^2\mu_d{}^2 - \alpha\,\eta^2\eta_d{}^2\mu_d\mu_h - \alpha\,\eta^2\eta_d{}^2\mu_d - \alpha\,\eta^2\eta_d{}^2\mu_h - \eta^4\mu_d\mu_h + \eta^2\mu_h \\ +4\,\eta^2\zeta_d\zeta_s\eta_d\mu_d + 4\,\eta^2\zeta_d\zeta_s\eta_d\mu_h + \eta^2\eta_d{}^2\mu_d{}^2 + \eta^2\eta_d{}^2\mu_d\mu_h - \eta^4\mu_d - \eta_d{}^2\mu_d \\ -\eta^4\mu_h + \eta^2\eta_d{}^2\mu_d + \eta^2\eta_d{}^2\mu_h + \alpha\,\eta_d{}^2\mu_d + \alpha\,\eta_d{}^2\mu_h + \eta^2\mu_d - \eta_d{}^2\mu_h \\ +2i\,(\mu_d+\mu_h)\,\eta\,\left(\zeta_s\,(\alpha-1)\,\eta_d{}^2 + \left(-1+(\mu_d+1)\,\eta^2\right)\zeta_d\eta_d + \eta^2\zeta_s\right),\end{array} \tag{54}$$

where $\eta = \omega/\omega_s$ refers to the ratio of excitation frequency to the natural frequency of the primary structure. To minimize the maximum displacement of the primary structure, the modulus of $H_s(\eta)$ is derived

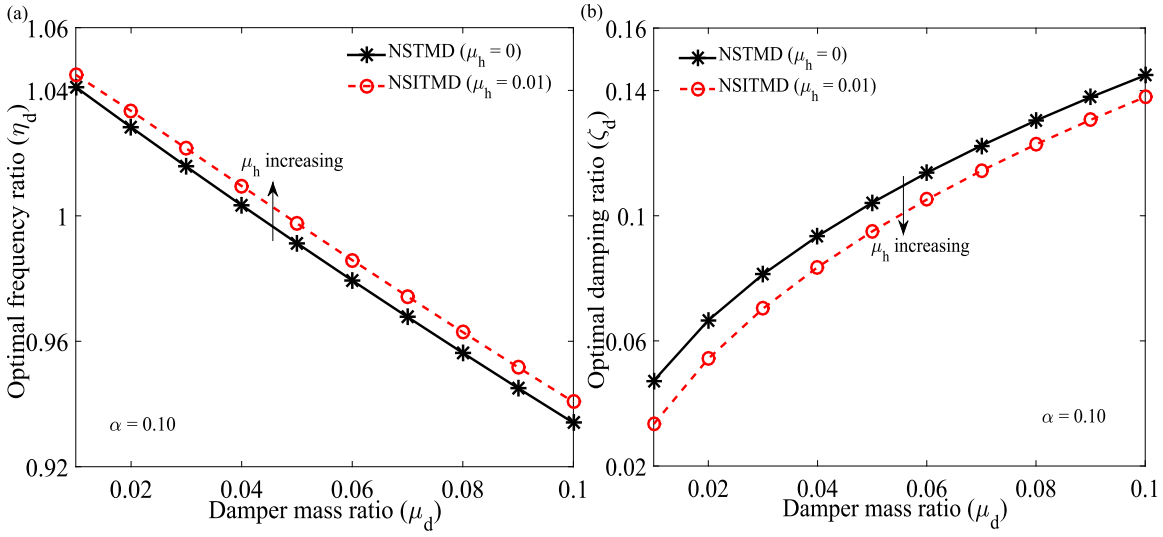

Fig. 19. (a) The differences in optimal frequency ratio η_d versus damper mass ratio μ_d for different values of inerter mass ratio μ_h of novel tuned mass dampers. The black solid ($\mu_h = 0$), red dashed ($\mu_h = 0.01$) lines with markers are employed to address plots for NSTMD and NSITMD. (b) The differences in optimal damping ratio ζ_d versus damper mass ratio μ_d for different values of inerter mass ratio μ_h of novel tuned mass dampers. The black solid ($\mu_h = 0$), red dashed ($\mu_h = 0.01$) lines with markers are employed to address plots for NSTMD and NSITMD. Eqs. (49) and (50) are applied to obtain both graphs. $\alpha = 0.10$ is considered for both graphs.

and expressed as

$$| H_s(\eta) | = \sqrt{\frac{A^2 + \zeta_d^2 B^2}{C^2 + \zeta_d^2 D^2}} = \left|\frac{B}{D}\right| \sqrt{\frac{\left(\frac{A}{B}\right)^2 + \zeta_d^2}{\left(\frac{C}{D}\right)^2 + \zeta_d^2}}. \tag{55}$$

The closed-form expression for A, B, C, and D are derived as

$$\begin{aligned}
A &= -\alpha\,\eta_d{}^2\mu_d{}^2 - \alpha\,\eta_d{}^2\mu_d\mu_h - \alpha\,\eta_d{}^2\mu_d - \alpha\,\eta_d{}^2\mu_h - \eta^2\mu_d\mu_h \\
&\quad + \mu_d{}^2\eta_d{}^2 + \eta_d{}^2\mu_d\mu_h - \eta^2\mu_d - \eta^2\mu_h + \eta_d{}^2\mu_d + \eta_d{}^2\mu_h, \\
B &= 2\,\eta\,\zeta_d\eta_d\mu_d{}^2 + 2\,\eta\,\zeta_d\eta_d\mu_d\mu_h + 2\,\eta\,\zeta_d\eta_d\mu_d + 2\,\eta\,\zeta_d\eta_d\mu_h, \\
C &= \begin{array}{c} -\alpha\,\eta^2\eta_d{}^2\mu_d{}^2 - \alpha\,\eta^2\eta_d{}^2\mu_d\mu_h - \alpha\,\eta^2\eta_d{}^2\mu_d \\ -\alpha\,\eta^2\eta_d{}^2\mu_h - \eta^4\mu_d\mu_h + \mu_d{}^2\eta^2\eta_d{}^2 \\ +\eta^2\eta_d{}^2\mu_d\mu_h - \eta^4\mu_d - \eta^4\mu_h + \eta^2\eta_d{}^2\mu_d + \eta^2\eta_d{}^2\mu_h + \alpha\,\eta_d{}^2\mu_d \\ +\alpha\,\eta_d{}^2\mu_h + \eta^2\mu_d \\ +\eta^2\mu_h - \eta_d{}^2\mu_d - \eta_d{}^2\mu_h \end{array}, \\
D &= 2\,\eta^3\zeta_d\eta_d\mu_d{}^2 + 2\,\eta^3\zeta_d\eta_d\mu_d\mu_h + 2\,\eta^3\zeta_d\eta_d\mu_d \\
&\quad + 2\,\eta^3\zeta_d\eta_d\mu_h - 2\,\eta\,\zeta_d\eta_d\mu_d - 2\,\eta\,\zeta_d\eta_d\mu_h.
\end{aligned} \tag{56}$$

Two constraints have been applied to derive the optimal frequency and damping ratio of the primary structure using the fixed point theory/ H_∞ optimization method [20,23]. The mathematical constraints are listed below.

$$\left(\frac{A}{B}\right)^2\Big|_\eta = \left(\frac{C}{D}\right)^2\Big|_\eta \quad \text{and} \quad \left(\frac{B}{D}\right)^2\Big|_{\eta_1} = \left(\frac{B}{D}\right)^2\Big|_{\eta_2}. \tag{57}$$

A closed-form expression has been derived from the first equation of Eq. (57) and expressed as [20]

$$+\begin{pmatrix} \left(2\,\mu_d{}^2\mu_h + 2\,\mu_d{}^2 + 4\,\mu_d\mu_h + 2\,\mu_d + 2\,\mu_h\right)\eta^4 \\ 2\,\alpha\,\eta_d{}^2\mu_d{}^3 + 2\,\alpha\,\eta_d{}^2\mu_d{}^2\mu_h + 4\,\alpha\,\eta_d{}^2\mu_d{}^2 + 4\,\alpha\,\eta_d{}^2\mu_d\mu_h \\ -2\,\eta_d{}^2\mu_d{}^3 - 2\,\mu_d{}^2\eta_d{}^2\mu_h + 2\,\alpha\,\eta_d{}^2\mu_d + 2\,\alpha\,\eta_d{}^2\mu_h \\ -4\,\mu_d{}^2\eta_d{}^2 - 4\,\eta_d{}^2\mu_d\mu_h - 2\,\eta_d{}^2\mu_d - 2\,\eta_d{}^2\mu_h \\ -\mu_d{}^2 - 2\,\mu_d\mu_h - 2\,\mu_d - 2\,\mu_h \\ -2\,\alpha\,\eta_d{}^2\mu_d{}^2 - 2\,\alpha\,\eta_d{}^2\mu_d\mu_h - 2\,\alpha\,\eta_d{}^2\mu_d - 2\,\alpha\,\eta_d{}^2\mu_h \\ +2\,\mu_d{}^2\eta_d{}^2 + 2\,\eta_d{}^2\mu_d\mu_h + 2\,\eta_d{}^2\mu_d + 2\,\eta_d{}^2\mu_h \end{pmatrix}\eta^2 = 0. \tag{58}$$

Another equation has also been derived using the second equation of Eq. (57) and expressed as

$$\eta_1^2 + \eta_2^2 = \frac{2}{\left(\mu_d + 1\right)}. \tag{59}$$

The closed-form expression for the optimal frequency ratio of NSITMD has been derived using Eq. (58) and expressed as

$$(\eta_d)_{opt} = \sqrt{\begin{array}{c} \dfrac{2\,\mu_d{}^2\mu_h + \mu_d{}^2 + 4\,\mu_d\mu_h + 2\,\mu_d + 2\,\mu_h - \mu_d{}^3}{6\,\mu_d{}^2 + 6\,\mu_d\mu_h + 2\,\mu_d + 2\,\mu_h - 2\,\alpha\,\mu_d{}^4} \\ -2\,\alpha\,\mu_d{}^3\mu_h - 6\,\alpha\,\mu_d{}^3 - 6\,\alpha\,\mu_d{}^2\mu_h \\ +2\,\mu_d{}^4 + 2\,\mu_d{}^3\mu_h - 6\,\alpha\,\mu_d{}^2 - 6\,\alpha\,\mu_d\mu_h \\ +6\,\mu_d{}^3 + 6\,\mu_d{}^2\mu_h - 2\,\alpha\,\mu_d - 2\,\alpha\,\mu_h \end{array}}. \tag{60}$$

The closed-form expressions for $\eta_{1,2}^2$ are derived as

$$\eta_{1,2}^2 = \frac{1 \pm \sqrt{1 + 4\,\left(\mu_d + 1\right)^4\left(\mu_h + \mu_d\right)(\alpha - 1)\left(\left(\mu_h\right)\mu_d + \mu_h\right)\eta_d{}^2}}{2\left(\mu_d + 1\right)^2\left(\left(\mu_h + 1\right)\mu_d + \mu_h\right)}. \tag{61}$$

Therefore, the optimal $\eta_{1,2}^2$ is derived by substituting Eq. (60) into Eq. (61) and expressed as

$$(\eta_{1,2}^2)_{opt} = \frac{1 \pm \sqrt{2\,\mu_d\left(\mu_d - 4\right)\left(\mu_d + 1\right)^3\mu_h + 2\,\mu_d{}^5 - 4\,\left(\mu_d + 1\right)^4\mu_h{}^2 - 6\,\mu_d{}^3 - 4\,\mu_d{}^2 + 1}}{2\left(\mu_d + 1\right)^2\left(\left(\mu_h + 1\right)\mu_d + \mu_h\right)}. \tag{62}$$

The mathematical expression for determining the closed-form expression for the optimal viscous damping ratio of NSITMD is derived as

$$\frac{\partial|H_s(\eta)|^2}{\partial\eta^2}|_{\eta_{1,2}^2} = 0 \quad \text{and} \quad (\zeta_d)_{opt} = \sqrt{\frac{\zeta_{d1}^2 + \zeta_{d2}^2}{2}}, \tag{63}$$

$$\begin{aligned} A_d\zeta_d^4 + B_d\zeta_d^2 + C_d &= 0 \\ \text{and} \quad \zeta_{d1,d2}^2 &= \frac{-B_d \pm \sqrt{B_d^2 - 4A_dC_d}}{2A_d}. \end{aligned} \tag{64}$$

The coefficients of ζ_d such as A_d, B_d, C_d are listed in Appendix B. The variations of the optimal frequency ratio versus the damper mass ratio of NSITMD for different values of negative stiffness ratio are shown in Fig. 20(a). To determine the graph, Eq. (60) is employed. The optimal

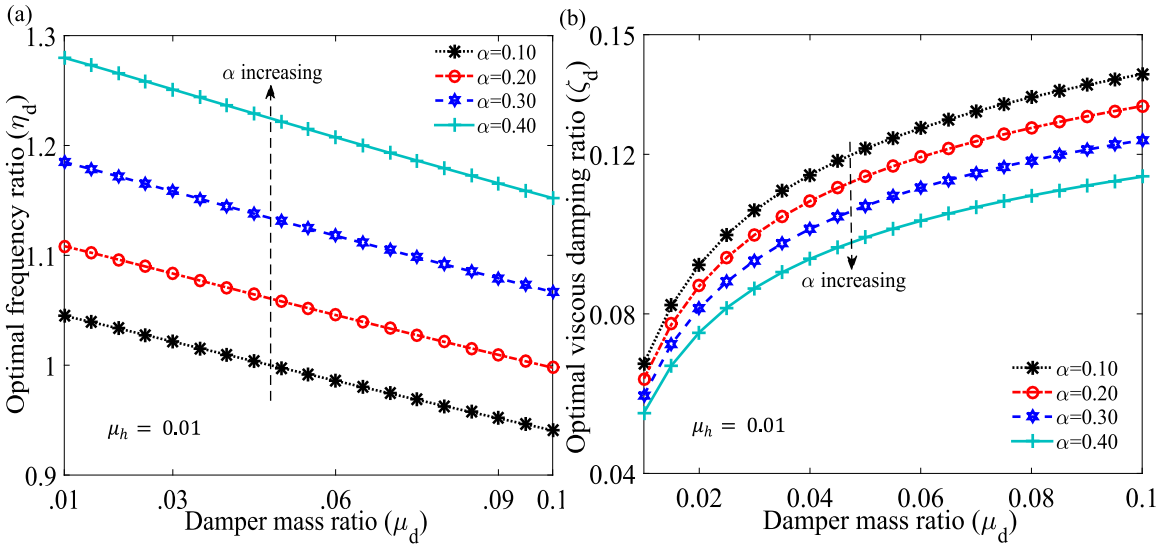

Fig. 20. (a) The variations of the optimal frequency ratio η_d versus the damper mass ratio μ_d of NSITMD for different values of negative stiffness ratio α. $\mu_h = 0.01$ and Eq. (60) are employed to determine the graph. (b) The variations of the optimal viscous damping ratio ζ_d versus the damper mass ratio μ_d of NSITMD for different values of negative stiffness ratio α. $\mu_h = 0.01$, Eqs. (63) and (64) are employed to determine the graph.

frequency ratio increases as the stiffness ratio increases and decreases as the damper mass ratio increases. A higher damper mass ratio, inerter mass ratio, and lower stiffness ratio have been recommended for achieving a flexible damper base with sufficient load-bearing capacity.

The variations of the optimal viscous damping ratio versus the damper mass ratio of NSITMD for different values of stiffness ratio are shown in Fig. 20(b). To obtain the graph, Eqs. (63) and (64) are employed. The optimal viscous damping ratio decreases as the stiffness ratio increases and slightly increases as the damper mass ratio increases. However, a higher stiffness ratio provides very lower damping, which can make the controlled structures under-damped. Moderate viscous damping ratios are affordable and easily implementable for practical applications. Therefore, a higher damper mass, inerter mass, and lower stiffness ratios have been recommended for achieving robust dynamic response reduction capacity at a moderate viscous damping range for NSITMD. The optimal closed-form solutions for optimal frequency and damping ratios of Negative stiffness tuned mass damper (NSTMD) are derived after $\mu_h = 0$ in Eqs. (60) and (64).

The variations of the optimal frequency ratio versus the damper mass ratio of NSTMD for different values of negative stiffness ratio are shown in Fig. 21(a). The optimal frequency ratio increases as the stiffness ratio increases and decreases as the damper mass ratio increases. A higher damper mass ratio and lower stiffness ratio are recommended for achieving a flexible base of the novel damper with sufficient load-bearing capacity. The variations of the optimal viscous damping ratio versus the base mass ratio of NSTMD for different values of negative stiffness ratio are shown in Fig. 21(b). The optimal viscous damping ratio decreases as the negative stiffness ratio increases and slightly increases as the damper mass ratio increases. A higher stiffness ratio provides very lower damping, which can make the isolated structures under-damped. Moderate viscous damping ratios are affordable and easily implementable for practical applications. Therefore, a higher damper mass and lower stiffness ratios have been recommended for achieving robust dynamic response reduction capacity at a moderate viscous damping range.

9. Robustness of NSITMD and NSTMD

The variations of optimal dynamic responses of the primary structure controlled by H_2 optimized NSITMD for different values of viscous damping ratio are shown in Fig. 22(a). $\mu_d = 0.05$, $\mu_h = 0.01$, $\alpha = 0.10$, $\zeta_s = 0$ are substituted in Eqs. (49) and (50), evaluating $(\eta_d)_{opt} = 0.9976$ and $(\zeta_d)_{opt} = 0.095$. $\eta = 0.8767, 1.075$ are the Eigen frequencies at $\zeta_d = 0$ and the anti-resonance frequency determines at $\eta = 0.9658$. $\eta = 0.8824, 1.06$ is the resonating frequency point; the maximum dynamic responses are mitigated at these frequency points. The minima frequency point is obtained at $\eta = 0.969$. At $\zeta_d = \infty$, the two degrees of freedom system dynamically behaves as a single degree of freedom system. $\eta = 0.9759$ is the frequency point for the response peak. The maximum dynamic response of the main structure is determined as 7.6539.

The variations of optimal dynamic responses of the primary structure controlled by H_∞ optimized NSITMD for different values of viscous damping ratio are shown in Fig. 22(b). $\mu_d = 0.05$, $\mu_h = 0.01$, $\alpha = 0.10$, $\zeta_s = 0$ are substituted in Eqs. (60), (63), and (64), evaluating $(\eta_d)_{opt} = 0.9976$ and $(\zeta_d)_{opt} = 0.1214$. $\eta = 0.8765, 1.075$ are the Eigen frequencies at $\zeta_d = 0$ and the anti-resonance frequency determines at $\eta = 0.9658$. $\eta = 0.903, 1.04$ is the resonating frequency point; the maximum dynamic responses are mitigated at these frequency points. The minima frequency point is obtained at $\eta = 0.9715$. At $\zeta_d = \infty$, the two degrees of freedom system dynamically behaves as a single degree of freedom system. $\eta = 0.9759$ is the frequency point for the response peak. The maximum dynamic response of the main structure is determined as 7.3379.

The variations of optimal dynamic responses of the primary structure controlled by H_2 optimized NSTMD for different values of viscous damping ratio are shown in Fig. 23(a). $\mu_d = 0.06$, $\mu_h = 0.0$, $\alpha = 0.10$, $\zeta_s = 0$ are substituted in Eqs. (49) and (50), evaluating $(\eta_d)_{opt} = 0.9794$ and $(\zeta_d)_{opt} = 0.1137$. $\eta = 0.852, 1.09$ are the Eigen frequencies at $\zeta_d = 0$ and the anti-resonance frequency determines at $\eta = 0.9563$. $\eta = 0.8579, 1.069$ is the resonating frequency point; the maximum dynamic responses are mitigated at these frequency points. The minima frequency point is obtained at $\eta = 0.9627$. At $\zeta_d = \infty$, the two degrees of freedom system dynamically behaves as a single degree of freedom system. $\eta = 0.9713$ is the frequency point for the response peak. The

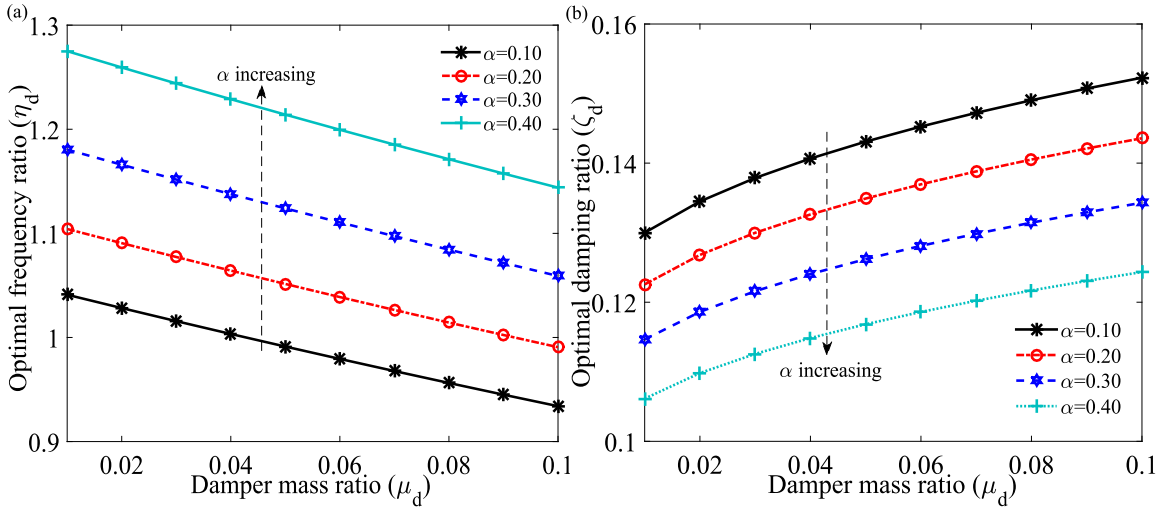

Fig. 21. (a) The variations of the optimal frequency ratio η_d versus the damper mass ratio μ_d of NSTMD for different values of negative stiffness ratio α. (b) The variations of the optimal viscous damping ratio ζ_d versus the damper mass ratio μ_d of NSTMD for different values of negative stiffness ratio α. $\mu_h = 0$, Eqs. (60), and (64) are employed to determine both graphs.

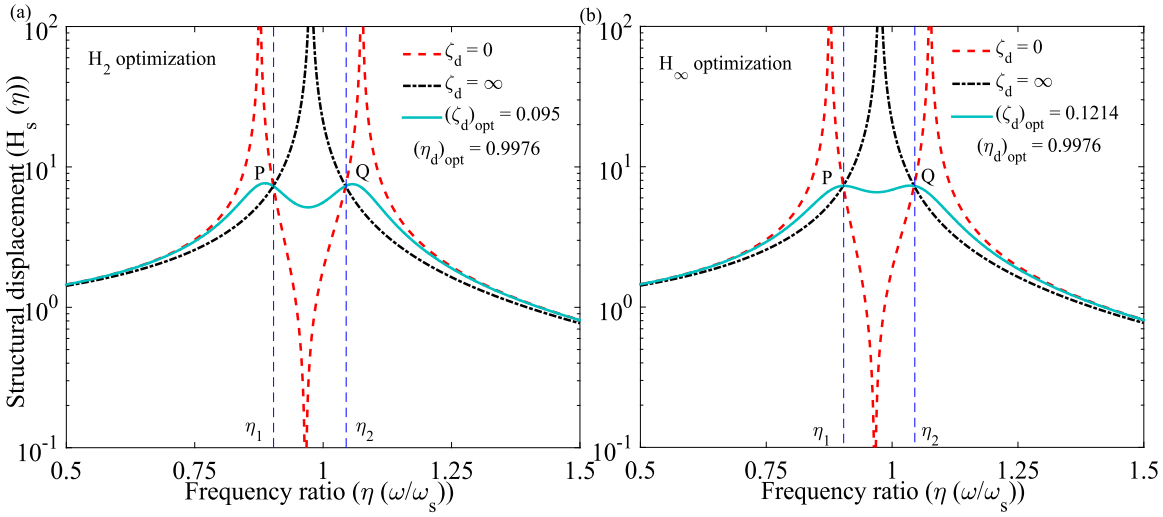

Fig. 22. (a) The differences in main structural optimal dynamic responses isolated by H_2 optimized NSITMD versus frequency ratio for various damping ratios. $\mu_d = 0.05$, $\mu_h = 0.01$, $\alpha = 0.10$, $\zeta_s = 0$ are considered system parameters. The optimal frequency and damping ratios are derived using Eqs. (49) and (50), i.e., $(\eta_d)_{opt} = 0.9976$ and $(\zeta_d)_{opt} = 0.095$. The red dashed ($\zeta_d = 0$), black dash-dotted ($\zeta_d = \infty$), and cyan solid ($(\zeta_d)_{opt} = 0.095$) lines are employed to address these plots. (b) The differences in main structural optimal dynamic responses isolated by H_∞ optimized NSITMD versus frequency ratio for various damping ratios. $\mu_d = 0.05$, $\mu_h = 0.01$, $\alpha = 0.10$, $\zeta_s = 0$ are considered system parameters. Eqs. (60), (63), and (64) are applied to derive the optimal frequency and damping ratios, i.e., $(\eta_d)_{opt} = 0.9976$ and $(\zeta_d)_{opt} = 0.1214$. The red dashed ($\zeta_d = 0$), black dash-dotted ($\zeta_d = \infty$), and sky blue solid ($(\zeta_d)_{opt} = 0.1214$) lines are employed to address these plots. P, Q, and R indicate the fixed points for both graphs.

maximum dynamic response of the main structure is determined as 6.4161.

The variations of optimal dynamic responses of the primary structure controlled by H_∞ optimized NSTMD for different values of viscous damping ratio are shown in Fig. 23(b). $\mu_d = 0.06$, $\mu_h = 0.0$, $\alpha = 0.10$, $\zeta_s = 0$ are substituted in Eqs. (60) and (64), evaluating $(\eta_d)_{opt} = 0.9794$ and $(\zeta_d)_{opt} = 0.1453$. $\eta = 0.8521, 1.09$ are the Eigen frequencies at $\zeta_d = 0$ and the anti-resonance frequency determines at $\eta = 0.9566$. $\eta = 0.8844, 1.043$ is the resonating frequency point; the maximum dynamic responses are mitigated at these frequency points. The minima frequency point is obtained at $\eta = 0.962$. At $\zeta_d = \infty$, the two degrees of freedom system dynamically behaves as a single degree of freedom system. $\eta = 0.9713$ is the frequency point for the response peak. The maximum dynamic response of the main structure is determined as 6.1497. H_2 optimized design parameters for novel and conventional tuned mass dampers are listed in Table 8.

Table 8
H_2 optimized design parameters for novel and conventional tuned mass dampers.

System	Proposed by	H_2 optimization	
		η_d	ζ_d
NSITMD	This study	Eq. (60)	Eq. (63), Eq. (64)
NSTMD ($\mu_h = 0$)	This study	Eq. (60)	Eq. (63), Eq. (64)
TMD	Iwata [50], Warburton et al. [51]	$\frac{1}{1+\gamma}\sqrt{\frac{2+\gamma}{2}}$	$\sqrt{\frac{\gamma(4+3\gamma)}{8(1+\gamma)(2+\gamma)}}$
TMD	Warburton et al. [51], Zilletti [52]	$\frac{1}{\sqrt{1+\gamma}}$	$\frac{\sqrt{\gamma}}{2}$

Where $\gamma = \mu_d + \mu_h = \mu_d$, i.e., the total static mass of TMD = NSITMD = NSTMD. TMD: $\gamma = 0.06$, NSITMD: $\mu_d + \mu_h = 0.05 + 0.01$, and NSTMD: $\mu_d + \mu_h = 0.05 + 0$.

The variations of optimal dynamic responses of uncontrolled structures and structures controlled by H_2 optimized NSITMD, H_2 optimized NSTMD, and H_2 optimized TMD Iwata [50], Warburton et al. [51] and Warburton et al. [51], Zilletti [52] versus frequency ratio for

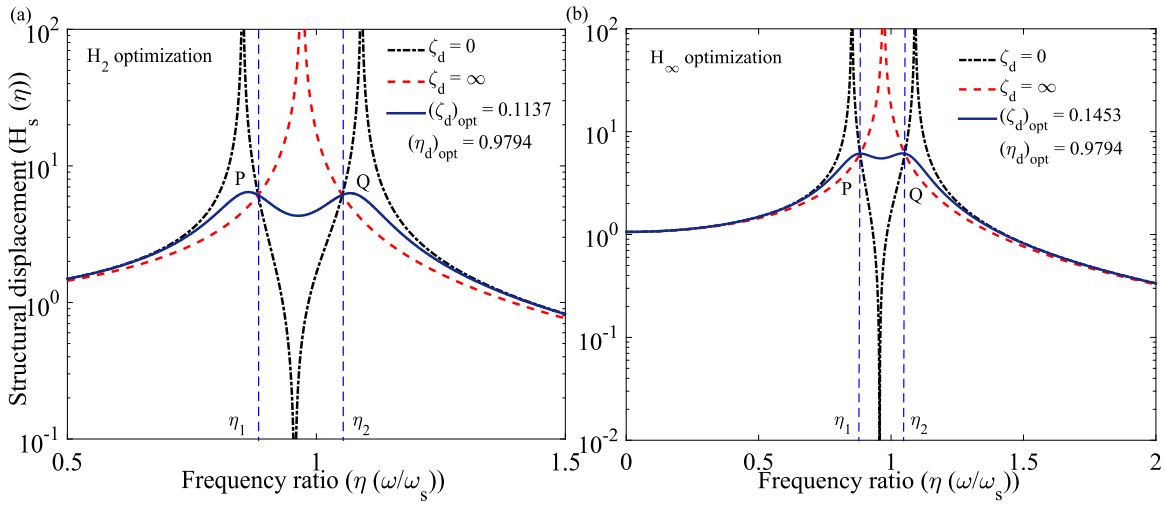

Fig. 23. (a) The differences in main structural optimal dynamic responses isolated by H_2 optimized NSTMD versus frequency ratio for various damping ratios. $\mu_d = 0.06$, $\mu_h = 0.0$, $\alpha = 0.10$, $\zeta_s = 0$ are considered system parameters. Eqs. (49) and (50) are applied to derive the optimal frequency and damping ratios, i.e., $(\eta_d)_{opt} = 0.9794$ and $(\zeta_d)_{opt} = 0.1137$. The black dash-dotted ($\zeta_d = 0$), red dashed ($\zeta_d = \infty$), and royal blue solid ($(\zeta_d)_{opt} = 0.1137$) lines are employed to address these plots. (b) The differences in main structural optimal dynamic responses isolated by H_∞ optimized NSTMD versus frequency ratio for various damping ratios. $\mu_d = 0.06$, $\mu_h = 0.0$, $\alpha = 0.10$, $\zeta_s = 0$ are considered system parameters. Eqs. (60), (63), and (64) are applied to derive the optimal frequency and damping ratios, i.e., $(\eta_d)_{opt} = 0.9794$ and $(\zeta_d)_{opt} = 0.1453$. The black dash-dotted ($\zeta_d = 0$), red dashed ($\zeta_d = \infty$), and royal blue solid ($(\zeta_d)_{opt} = 0.1453$) lines are employed to address these plots. P, Q, and R indicate the fixed points for both graphs.

Table 9
The system parameters of main structures (uncontrolled and controlled structures).

Name	Symbol	Values
Damping ratio	ζ_s	0.05

different damping ratio values are displayed in Figs. 24(a) and 24(b). $\zeta_s = 0.05$ is the damping ratio of the main structure. The system parameter for the main structure is listed in Table 9. The maximum dynamic response of the uncontrolled structure is determined as 10.0125. The maximum dynamic responses of the structures controlled by H_2 optimized TMD developed by Iwata [50], Warburton et al. [51] and Warburton et al. [51], Zilletti [52] are derived as 5.3049 and 5.5314. The maximum dynamic responses of the structures controlled by H_2 optimized NSITMD and NSTMD are determined as 5.2821 and 4.786. H_2 optimized NSITMD is 0.42% and 10.84% superior to H_2 optimized TMD developed by Iwata [50], Warburton et al. [51]. H_2 optimized NSTMD is 4.5% and 13.48% superior to H_2 optimized TMD developed by Warburton et al. [51], Zilletti [52].

10. Conclusions

The negative stiffness inerter-based base isolator (NSIBI), negative stiffness base-isolated (NSBI), negative stiffness inerter-based tuned mass damper (NSITMD), and negative stiffness tuned mass dampers (NSTMD) are introduced in this paper. H_2 and H_∞ optimization methods are applied to derive the optimal design parameters for these novel passive vibration control devices in terms of closed-form expressions. The transfer function formation and Newmark-beta method are applied to determine dynamic responses of the controlled structures analytically and numerically. The parametric study shows that the effective mass and stiffness ratios increase as the base and inerter mass ratios increase for the NSIBI ($\mu_d \neq 0$) system. In contrast, the effective stiffness decreases as the negative stiffness ratio of NSBI ($\mu_d = 0$) increases. The optimal frequency ratio decreases as the base mass ratio of H_2 and H_∞ optimized NSIBI and NSBI increase. However, it increases as the negative stiffness ratio increases. In addition, optimal damping ratios decrease when the base mass and negative stiffness ratio increase. For H_2 and H_∞ optimized NSITMD ($\mu_h \neq 0$) and NSTMD ($\mu_h = 0$), the optimal frequency ratio decreases and increases when the damper and negative stiffness ratios increase. In addition, the optimal damping ratio increases and decreases when the damper and negative stiffness ratios increase. The dynamic response reduction capacity of each novel damper is determined. Therefore, H_2 optimized NSIBI and NSBI are 45.98% and 46.71% superior to optimum TBI. Whereas H_∞ optimized NSIBI and NSBI are 58.36% and 57.32% superior to optimum TBI. Whereas H_2 optimized NSITMD is 0.42% and 10.84% superior to H_2 optimized TMD developed by Iwata [50], Warburton et al. [51]. H_2 optimized NSTMD is 4.5% and 13.48% superior to H_2 optimized TMD developed by Warburton et al. [51], Zilletti [52]. The paper's novelty lies in introducing negative stiffness inerter passive dampers and their corresponding optimal design parameters. These novel passive dampers are cost-effective. The proposed dampers' practical realization, experimentation, and prototyping are the research's future scope.

CRediT authorship contribution statement

Sudip Chowdhury: Conceptualization, Formal analysis, Investigation, Resources, Methodology, Software, Data curation, Writing – original draft, Visualization, Investigation, Critical discussion, Reviewing & editing. **Arnab Banerjee:** Visualization, Supervision, Funding acquisition, Reviewing, Resources. **Sondipon Adhikari:** Visualization, Supervision, Reviewing, Discussion, Methodology.

Declaration of competing interest

The authors declare that they have no known competing financial interests or personal relationships that could have appeared to influence the work reported in this paper.

Data availability

No data was used for the research described in the article

Acknowledgments

The authors would like to acknowledge the Inspire faculty grant, grant number DST/INSPIRE/04/2018/000052 for partial financial support for the project. SC would like to acknowledge the MHRD grant received from IIT Delhi during the period of this research work.

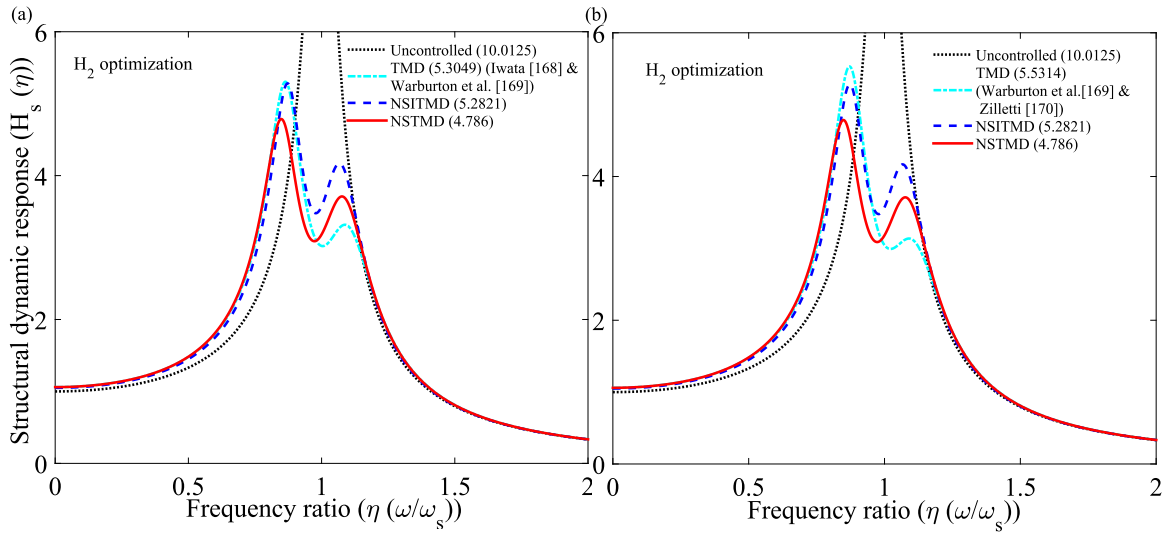

Fig. 24. The variations of optimal dynamic responses of uncontrolled structures and structures controlled by H_2 optimized NSITMD, H_2 optimized NSTMD, and H_2 optimized TMD ((a) Iwata [50], Warburton et al. [51] and (b) Warburton et al. [51], Zilletti [52]) versus frequency ratio for different damping ratio values. The black dotted (uncontrolled), cyan dash-dotted (TMD), blue dashed (NSITMD), and red solid (NSTMD) Tables 8 and 9 are applied for both graphs.

Appendix A. The closed-form expressions for A_1, B_1, and C_1 from Eq. (31)

$$A_1 = -128\,\eta_{1,2}^4\left(\mu_b + 2\,\mu_d - 1\right)^2\left(\mu_b + \mu_d\right)^2\left(\eta_{1,2}^2 - 1\right). \tag{A.1}$$

$$B_1 = -96\begin{pmatrix} \left(4/3\,{\mu_d}^2 + 2\,\mu_b\mu_d + {\mu_b}^2\right)\eta_{1,2}^6 \\ +\left(-2/3\,{\mu_b}^2 + 4/3\,{\mu_d}^2 - 2\,\mu_b - 8/3\,\mu_d\right)\eta_{1,2}^4 \\ +\left(\left(-2/3\,\mu_d + 1/3\right)\mu_b - 4/3\,{\mu_d}^2 + 1\right)\eta_{1,2}^2 \\ -1/3\,\left(\mu_b + 2\,\mu_d - 1\right)^2 \\ (\beta - 1)\left(\mu_b + 2\,\mu_d - 1\right)\left(\mu_b + \mu_d\right)\eta_{1,2}^2 \end{pmatrix}. \tag{A.2}$$

$$C_1 = \begin{pmatrix} \left(\left(\mu_d + \mu_b\right)\eta_{1,2}^4 + \left(-1/2\,\mu_b - 3/2\right)\eta_{1,2}^2 - 1/2\,\mu_b - \mu_d + 1/2\right) \\ -32\,(-1+\beta)^2\left(\eta_{1,2}^2\mu_d + 1/2\,\mu_b + \mu_d - 1/2\right) \\ \left(\left(\mu_d + \mu_b\right)\mu_d\eta_{1,2}^4 + \left(\mu_b - 1 + 2\,\mu_d\right)\left(\mu_d + \mu_b\right)\eta_{1,2}^2\right) \\ -1/4\,\left(\mu_b - 1 + 2\,\mu_d\right)\left(\mu_b - 2\,\mu_d + 3\right) \end{pmatrix}. \tag{A.3}$$

Appendix B. The closed-form expression for A_d, B_d, and C_d from Eq. (64)

$$A_d = 64\left(\eta_{1,2}^2\mu_d + \eta_{1,2}^2 - 1\right)\left(\mu_d + \mu_h\right)^2\left(\mu_d + 1\right)^4\eta_{1,2}^4 \left({\mu_d}^2 + \left(-2\,\mu_h - 2\right)\mu_d - 2\,\mu_h\right)^2. \tag{B.1}$$

$$B_d = \begin{pmatrix} 64\left(\mu_d + 1\right)^2(\alpha - 1)\left(\mu_d + \mu_h\right) \\ \left({\mu_d}^2 + \left(-2\,\mu_h - 2\right)\mu_d - 2\,\mu_h\right)\eta_{1,2}^2\left(\eta_{1,2}^2\mu_d + \eta_{1,2}^2 - 1\right) \\ \begin{pmatrix} \left(1/4 + \eta_{1,2}^4{\mu_h}^2 + 2\,\eta_{1,2}^4\mu_h + \eta_{1,2}^4\right){\mu_d}^4 \\ +4\begin{pmatrix} \left(\eta_{1,2}^4 - \eta_{1,2}^2/2\right)\mu_h + 1/2\,\eta_{1,2}^4 \\ -\eta_{1,2}^2/2 - 1/4 \end{pmatrix}\left(\mu_h + 1\right){\mu_d}^3 \\ +\begin{pmatrix} \left(6\,\eta_{1,2}^4 - 6\,\eta_{1,2}^2 + 1\right){\mu_h}^2 \\ +\left(6\,\eta_{1,2}^4 - 8\,\eta_{1,2}^2 + 1\right)\mu_h \\ +\left(\eta_{1,2}^2 - 1\right)^2 \end{pmatrix}{\mu_d}^2 \\ +4\left(\left(\eta_{1,2}^2 - 1/2\right)\mu_h + \eta_{1,2}^2/2 - 1/2\right) \\ \mu_h\left(\eta_{1,2}^2 - 1\right)\mu_d + {\mu_h}^2\left(\eta_{1,2}^2 - 1\right)^2 \end{pmatrix} \end{pmatrix}. \tag{B.2}$$

$$\begin{aligned} C_d =& 16\left(\mu_d\mu_h + \mu_d + \mu_h\right)^4(\alpha - 1)^2\left(\mu_d + 1\right)^5\eta_{1,2}^{10} \\ &+ 16\begin{pmatrix} \left(\left(\mu_h + 1\right)\mu_d + \mu_h\right)^3(\alpha - 1)^2\left(\mu_d + 1\right)^4 \\ {\mu_d}^2 + \left(-5\,\mu_h - 5\right)\mu_d - 5\,\mu_h \end{pmatrix}\eta_{1,2}^8 \\ &- 8\begin{pmatrix} \left({\mu_d}^2 + \left(10\,\mu_h + 10\right)\mu_d + 10\,\mu_h\right)\left(\left(\mu_h + 1\right)\mu_d + \mu_h\right)^2 \\ \left({\mu_d}^2 + \left(-2\,\mu_h - 2\right)\mu_d - 2\,\mu_h\right)\left(\mu_d + 1\right)^3(\alpha - 1)^2 \end{pmatrix}\eta_{1,2}^6 \\ &- 4\begin{pmatrix} \left(\left(\mu_h + 1\right)\mu_d + \mu_h\right) \\ \begin{pmatrix} {\mu_d}^4 + \left(2\,\mu_h + 2\right){\mu_d}^3 \\ +\left(-20\,{\mu_h}^2 - 38\,\mu_h - 20\right){\mu_d}^2 \\ +\left(-40\,{\mu_h}^2 - 40\,\mu_h\right)\mu_d - 20\,{\mu_h}^2 \end{pmatrix} \\ \left({\mu_d}^2 + \left(-2\,\mu_h - 2\right)\mu_d - 2\,\mu_h\right) \\ \left(\mu_d + 1\right)^2(\alpha - 1)^2 \end{pmatrix}\eta_{1,2}^4 \\ &+ \begin{pmatrix} \left({\mu_d}^2 + \left(-2\,\mu_h - 2\right)\mu_d - 2\,\mu_h\right)^2\left(\mu_d + 1\right)(\alpha - 1)^2 \\ \begin{pmatrix} {\mu_d}^4 + \left(4\,\mu_h + 4\right){\mu_d}^3 \\ +\left(20\,{\mu_h}^2 + 44\,\mu_h + 20\right){\mu_d}^2 \\ +\left(40\,{\mu_h}^2 + 40\,\mu_h\right)\mu_d + 20\,{\mu_h}^2 \end{pmatrix} \end{pmatrix}\eta_{1,2}^2 \\ &- 16\,\alpha\,{\mu_h}^4(\alpha - 2). \end{aligned} \tag{B.3}$$

References

[1] Kelly JM. Base isolation: Linear theory and design. Earthq Spectra 1990;6(2):223–44.

[2] Asami T, Nishihara O, Baz AM. Analytical solutions to H_∞ and H_2 optimization of dynamic vibration absorbers attached to damped linear systems. J Vib Acoust 2002;124(2):284–95.

[3] Chen Z, Jiang R, Wang RY, Chen T. Active TMD systematic design of fuzzy control and the application in high-rise buildings. Earthq Struct 2021;21(6):577–85.

[4] Touaillon J. Improvement in buildings. 1870, Google Patents U.S. Patent No. 99, 973.

[5] Zhang W, Zhao J. Analysis on nonlinear stiffness and vibration isolation performance of scissor-like structure with full types. Nonlinear Dynam 2016;86(1):17–36.

[6] Cheng X, Jing W, Gong L. Simplified model and energy dissipation characteristics of a rectangular liquid-storage structure controlled with sliding base isolation and displacement-limiting devices. J Perform Construct Facil 2017;31(5):04017071.

[7] Furinghetti M, Pavese A, Quaglini V, Dubini P. Experimental investigation of the cyclic response of double curved surface sliders subjected to radial and bidirectional sliding motions. Soil Dyn Earthq Eng 2019;117:190–202.

[8] Hwang J, Chiou J. An equivalent linear model of lead-rubber seismic isolation bearings. Eng Struct 1996;18(7):528–36.
[9] Nguyen XB, Komatsuzaki T, Truong HT. Adaptive parameter identification of Bouc-Wen hysteresis model for a vibration system using magnetorheological elastomer. Int J Mech Sci 2022;213:106848.
[10] Buckle IG. New Zealand seismic base isolation concepts and their application to nuclear engineering. Nucl Eng Des 1985;84(3):313–26.
[11] Robinson WH. Lead-rubber hysteretic bearings suitable for protecting structures during earthquakes. Earthq Eng Struct Dynam 1982;10(4):593–604.
[12] Jangid R. Computational numerical models for seismic response of structures isolated by sliding systems. Struct Control Health Monit 2005;12(1):117–37.
[13] Jangid R. Optimum friction pendulum system for near-fault motions. Eng Struct 2005;27(3):349–59.
[14] Shakib H, Fuladgar A. Response of pure-friction sliding structures to three components of earthquake excitation. Comput Struct 2003;81(4):189–96.
[15] Chowdhury S. Nonlinear dynamic analysis of torsionally coupled isolated structures. Pract Period Struct Des Construct 2021;26(3):04021023.
[16] Frahm H. Devices for damping vibration of bodies. 1909, US Patent 989958.
[17] Pietrosanti D, De Angelis M, Basili M. A generalized 2-DOF model for optimal design of MDOF structures controlled by Tuned Mass Damper Inerter (TMDI). Int J Mech Sci 2020;185:105849.
[18] Ormondroyd J. The theory of the dynamic vibration absorber. Trans ASME Appl Mech 1928;50:9–22.
[19] Chowdhury S, Banerjee A. The exact closed-form expressions for optimal design parameters of resonating base isolators. Int J Mech Sci 2022;107284.
[20] Chowdhury S, Banerjee A, Adhikari S. Optimal negative stiffness inertial-amplifier-base-isolators: Exact closed-form expressions. Int J Mech Sci 2022;107044.
[21] Cheng Z, Palermo A, Shi Z, Marzani A. Enhanced tuned mass damper using an inertial amplification mechanism. J Sound Vib 2020;115267.
[22] Baduidana M, Kenfack-Jiotsa A. Optimal design of inerter-based isolators minimizing the compliance and mobility transfer function versus harmonic and random ground acceleration excitation. J Vib Control 2021;27(11–12):1297–310.
[23] Den Hartog JP. Mechanical vibrations. Courier Corporation; 1985.
[24] Batou A, Adhikari S. Optimal parameters of viscoelastic tuned-mass dampers. J Sound Vib 2019;445:17–28.
[25] Smith MC. The inerter: A retrospective. Annu Rev Control Robot Autonom Syst 2020;3:361–91.
[26] Smith MC. Synthesis of mechanical networks: The inerter. IEEE Trans Automat Control 2002;47(10):1648–62.
[27] Smith MC, Wang F-C. Performance benefits in passive vehicle suspensions employing inerters. Veh Syst Dynam 2004;42(4):235–57.
[28] Banerjee A, Adhikari S, Hussein MI. Inertial amplification band-gap generation by coupling a levered mass with a locally resonant mass. Int J Mech Sci 2021;207:106630.
[29] Adhikari S, Banerjee A. Enhanced low-frequency vibration energy harvesting with inertial amplifiers. J Intell Mater Syst Struct 2021. 1045389X211032281.
[30] Chowdhury S, Banerjee A, Adhikari S. The optimum enhanced viscoelastic tuned mass dampers: Exact closed-form expressions. J Vib Control 2023;10775463231156240.
[31] Yilmaz C, Hulbert GM, Kikuchi N. Phononic band gaps induced by inertial amplification in periodic media. Phys Rev B 2007;76(5):054309.
[32] Marian L, Giaralis A. Optimal design of a novel Tuned Mass-Damper–Inerter (TMDI) passive vibration control configuration for stochastically support-excited structural systems. Probab Eng Mech 2014;38:156–64.
[33] Zhao Z, Chen Q, Zhang R, Pan C, Jiang Y. Optimal design of an inerter isolation system considering the soil condition. Eng Struct 2019;196:109324.
[34] Čakmak D, Tomičević Z, Wolf H, Božić Ž, Semenski D, Trapić I. Vibration fatigue study of the helical spring in the base-excited inerter-based isolation system. Eng Fail Anal 2019;103:44–56.
[35] Petrini F, Giaralis A, Wang Z. Optimal Tuned Mass-Damper-Inerter (TMDI) design in wind-excited tall buildings for occupants' comfort serviceability performance and energy harvesting. Eng Struct 2020;204:109904.
[36] Muscolino G, Palmeri A, Versaci C. Damping-adjusted combination rule for the response spectrum analysis of base-isolated buildings. Earthq Eng Struct Dynam 2013;42(2):163–82.
[37] Carrella A, Brennan M, Waters T. Static analysis of a passive vibration isolator with quasi-zero-stiffness characteristic. J Sound Vib 2007;301(3–5):678–89.
[38] Cheng C, Li S, Wang Y, Jiang X. On the analysis of a high-static-low-dynamic stiffness vibration isolator with time-delayed cubic displacement feedback. J Sound Vib 2016;378:76–91.
[39] Huang X, Liu X, Sun J, Zhang Z, Hua H. Vibration isolation characteristics of a nonlinear isolator using Euler buckled beam as negative stiffness corrector: A theoretical and experimental study. J Sound Vib 2014;333(4):1132–48.
[40] Iemura H, Pradono MH. Advances in the development of pseudo-negative-stiffness dampers for seismic response control. Struct Control Health Monit: Off J Int Assoc Struct Control Monit Eur Assoc Control Struct 2009;16(7–8):784–99.
[41] Lakes RS, Lee T, Bersie A, Wang Y-C. Extreme damping in composite materials with negative-stiffness inclusions. Nature 2001;410(6828):565–7.
[42] Shi X, Zhu S. Simulation and optimization of magnetic negative stiffness dampers. Sensors Actuators A 2017;259:14–33.
[43] Kapasakalis KA, Antoniadis IA, Sapountzakis EJ. Performance assessment of the KDamper as a seismic absorption base. Struct Control Health Monit 2020;27(4):e2482.
[44] Kapasakalis KA, Antoniadis IA, Sapountzakis EJ. STIFF vertical seismic absorbers. J Vib Control 2022;28(15–16):1937–49.
[45] Kapasakalis KA, Antoniadis IA, Sapountzakis EJ. Constrained optimal design of seismic base absorbers based on an extended KDamper concept. Eng Struct 2021;226:111312.
[46] Kapasakalis KA, Antoniadis IA, Sapountzakis EJ, Kampitsis AE. Vibration mitigation of wind turbine towers using negative stiffness absorbers. J Civ Eng Construct 2021;10(3):123–39.
[47] Xiang S, Songye Z. A comparative study of vibration isolation performance using negative stiffness and inerter dampers. J Franklin Inst B 2019;356(14):7922–46.
[48] Matsagar VA, Jangid R. Seismic response of base-isolated structures during impact with adjacent structures. Eng Struct 2003;25(10):1311–23.
[49] Chowdhury S, Banerjee A. The exact closed-form equations for optimal design parameters of enhanced inerter-based isolation systems. J Vib Control 2022;10775463221133428.
[50] Iwata Y. On the construction of the dynamic vibration absorbers. Japan Soc Mech Eng 1982;820(8):150–2.
[51] Warburton GB. Optimum absorber parameters for various combinations of response and excitation parameters. Earthq Eng Struct Dynam 1982;10(3):381–401.
[52] Zilletti M, Elliott SJ, Rustighi E. Optimisation of dynamic vibration absorbers to minimise kinetic energy and maximise internal power dissipation. J Sound Vib 2012;331(18):4093–100.